
Research Articles: Development/Plasticity/Repair

Cenpj regulates cilia disassembly and neurogenesis in the developing mouse cortex

Wenyu Ding^{1,2}, Qian Wu^{1,2}, Le Sun^{1,2}, Na Clara Pan^{1,2} and Xiaoqun Wang^{1,2,2}

¹*State Key Laboratory of Brain and Cognitive Science, CAS Center for Excellence in Brain Science and Intelligence Technology (Shanghai), Institute of Biophysics, Chinese Academy of Sciences, Beijing, 100101, China*

²*University of Chinese Academy of Sciences, Beijing 100049, China*

³*Beijing Institute for Brain Disorders, Beijing 100069, China*

<https://doi.org/10.1523/JNEUROSCI.1849-18.2018>

Received: 20 July 2018

Revised: 19 December 2018

Accepted: 24 December 2018

Published: 9 January 2019

Author contributions: W.D., Q.W., and X.W. designed research; W.D., Q.W., L.S., N.C.P., and X.W. performed research; W.D., Q.W., L.S., N.C.P., and X.W. analyzed data; W.D., Q.W., L.S., N.C.P., and X.W. edited the paper; W.D., Q.W., and X.W. wrote the paper; Q.W. and X.W. wrote the first draft of the paper; X.W. contributed unpublished reagents/analytic tools.

Conflict of Interest: The authors declare no competing financial interests.

We gratefully acknowledge Dr. Bradley Yoder (University of Alabama at Birmingham) kindly shared and transferred the mouse strain to us. We thank Dr. Tian Xue (University of Science and Technology of China) for sharing ARPE19 cell line with us. We also thank Jianguo Zhang, Lei Sun and Can Peng of the Center for Biological Imaging, Institute of Biophysics, CAS for their help in making EM sample and taking EM images. We thank Dr. Arnold Kriegstein (University of California at San Francisco) and his lab members for their generous discussion and reagent support. This work was supported by the National Basic Research Program of China (2017YFA0103303, 2017YFA0102601); the Strategic Priority Research Program of the Chinese Academy of Sciences (grant number XDA16020601); National Natural Science Foundation of China (NSFC) (31371100) and Newton Advanced Fellowship (grant number NA140416) to X. W.

Corresponding author: Xiaoqun Wang (xiaoqunwang@ibp.ac.cn)

Cite as: J. Neurosci 2019; 10.1523/JNEUROSCI.1849-18.2018

Alerts: Sign up at www.jneurosci.org/alerts to receive customized email alerts when the fully formatted version of this article is published.

Accepted manuscripts are peer-reviewed but have not been through the copyediting, formatting, or proofreading process.

-
- 1 **Cenpj regulates cilia disassembly and neurogenesis in the developing**
2 **mouse cortex**
- 3 Abbreviated Title: Cilia and neurogenesis regulated by Cenpj
- 4 Wenyu Ding^{1,2,*}, Qian Wu^{1,2,*}, Le Sun^{1,2}, Na Clara Pan^{1,2} and Xiaoqun Wang^{1,2,3,#}
- 5
- 6 ¹State Key Laboratory of Brain and Cognitive Science, CAS Center for Excellence in
- 7 Brain Science and Intelligence Technology (Shanghai), Institute of Biophysics,
- 8 Chinese Academy of Sciences, Beijing, 100101, China
- 9 ²University of Chinese Academy of Sciences, Beijing 100049, China
- 10 ³Beijing Institute for Brain Disorders, Beijing 100069, China
- 11
- 12 *These authors contributed equally to this work.
- 13 # Corresponding author: Xiaoqun Wang (xiaoqunwang@ibp.ac.cn)
- 14
- 15
- 16
- 17
- 18 Number of pages: 49
- 19 The manuscript includes 9 figures and 6 movies.
- 20 Title 11 words; Abbreviated Title 41 characters (including spaces); Abstract **185**
- 21 words; Significance Statement **152** words; Introduction 593 words; Discussion **1323**
- 22 words.

23 **Author contributions**

24 W. D., Q. W. and X. W. conceived the project, designed the experiments and wrote the
25 manuscript. W. D. and Q. W. conducted the experiments, including animal surgery,
26 tissue preparation, immunostaining, and imaging. N. C. P. cultured the cells. L. S.
27 performed RNA-seq data analysis and interpretation. All the authors edited and
28 proved the manuscript.

29

30 **Acknowledgments**

31 We gratefully acknowledge Dr. Bradley Yoder (University of Alabama at Birmingham)
32 kindly shared and transferred the mouse strain to us. We thank Dr. Tian Xue
33 (University of Science and Technology of China) for sharing ARPE19 cell line with
34 us. We also thank Jianguo Zhang, Lei Sun and Can Peng of the Center for Biological
35 Imaging, Institute of Biophysics, CAS for their help in making EM sample and taking
36 EM images. We thank Dr. Arnold Kriegstein (University of California at San
37 Francisco) and his lab members for their generous discussion and reagent support.

38 This work was supported by the National Basic Research Program of China
39 (2017YFA0103303, 2017YFA0102601); the Strategic Priority Research Program of
40 the Chinese Academy of Sciences (grant number XDA16020601); National Natural
41 Science Foundation of China (NSFC) (31371100) and Newton Advanced Fellowship
42 (grant number NA140416) to X. W.

43 **Competing financial interests**

44 The authors declare no competing financial interests.

45 **Abstract**

46 Primary cilia are microtubule-based protuberances that project from the eukaryotic
47 cell body to sense the extracellular environment. Ciliogenesis is closely correlated to
48 the cell cycle, and defects of cilia are related to human systemic diseases, such as
49 primary ciliary dyskinesia. However, the role of ciliogenesis in cortical development
50 remains unclear. Here, we demonstrate that Cenpj, a protein that is required for
51 centriole biogenesis, plays a role in regulating cilium disassembly *in vivo*. Depletion
52 of Cenpj in neural progenitor cells results in long cilia and abnormal cilium disassembly.
53 Radial glial cells (RG cells) with Cenpj depletion exhibit uncompleted cell division,
54 reduced cell proliferation and increased cell apoptosis in the developing mouse
55 cerebrum cortex, leading to microcephaly. In addition, Cenpj depletion causes long
56 and thin primary cilia and motile cilia in adult neural stem cells and reduced cell
57 proliferation in the subventricular zone (SVZ). Furthermore, we show that Cenpj
58 regulates cilium disassembly and neurogenesis through Kif2a, a plus-end-directed motor
59 protein. These data, collected from mice of both sexes, provide insights into how
60 ciliogenesis plays roles in cortical development and primary microcephaly induced by
61 *Cenpj* mutations in humans.

62

63

64

65

66

67 **Significance Statement**

68 Autosomal recessive primary microcephaly (MCPH) is a neurodevelopmental
69 disorder showing the major symptoms of reduction of circumference of the head,
70 brain volume and cortex thickness with normal brain architecture in birth. We used
71 conditional Cenpj deletion mice and found that neural progenitor cells exhibited long
72 primary cilia and abnormal cilium appendages. The defective cilium disassembly
73 caused by Cenpj depletion might correlate to reduced cell proliferation, uncompleted
74 cell division, cell apoptosis, and microcephaly in mice. Cenpj also regulates cilium
75 structure of adult neural stem cells and adult neurogenesis in mice. Additionally, our
76 results illustrated that Cenpj regulated cilia disassembly and neurogenesis through
77 Kif2a, indicating that primary cilia dynamic plays a crucial role in neural progenitor
78 cell mitosis and adult neurogenesis.

79

80

81

82

83

84

85

86

87

88

89 Introduction

90 Centrosomes are the organelles at the poles of the spindle that can persist into
91 interphase as microtubule organizing centers (MTOCs). The core is a ninefold
92 symmetrical centriole, and their ability to nucleate cytoplasmic microtubules (MTs) is
93 a property of the surrounding pericentriolar material (PCM). The centriole has a dual
94 life, existing not only as the core of the centrosome but also as the basal body for
95 primary cilia assembly. As a result, the structure and function of the centriole, the
96 centrosome, and the cilia have an impact on many aspects of development and
97 physiology. The primary cilium, a continuation and extension of microtubule doublets
98 from the basal body structure, is localized to the apical region of a radial glial cell
99 (RG cell). In the G0 quiescent phase, the RG cell processes a primary cilium out of
100 the ventricular endfoot surface. Upon entry into the cell cycle, the primary cilium
101 disassembles quickly to release the centrioles to form a bipolar spindle (Kobayashi
102 and Dynlach, 2011; Nigg and Stearns, 2011). Cilium assembly and disassembly are
103 highly correlated to the cell cycle and centrosome (Pugacheva et al., 2007; Qin et al.,
104 2007; Robert et al., 2007). The dynamics of primary cilia, unique in their ability to
105 function as sensors and conveyors of critical signals in a complex environment, may
106 have a supervisory role in the neurogenesis of RG cells.

107 Mutations of Cenpj or CPAP (a centrosomal-P4.1-associated protein) cause
108 microcephaly, dwarfism, low birthweight, and intellectual disability (Al-Dosari et al.,
109 2010), which are thought to arise from a decline in neural progenitor cells (NPCs)
110 during development (Insolera et al., 2014b). Depletion of Cenpj causes severe defects

111 in centriole duplication and increases the population of monopolar, asymmetric
112 bipolar, and multipolar spindles in mitotic cells (Cho et al., 2006b; Kitagawa et al.,
113 2011a; Kohlmaier et al., 2009; Schmidt et al., 2009; Tang et al., 2009a). In addition,
114 Cenpj acts as a scaffold for the cilium disassembly complex (CDC), which includes
115 Nde1, Aurora A, and OFD1, that is recruited to the ciliary base for timely cilium
116 disassembly(Gabriel et al., 2016). Mouse embryos with complete elimination of
117 Cenpj present prolonged mitosis and a widespread, p53-dependent cell death
118 phenotype, resulting in a reduction in RG cells and other types of neural progenitor
119 cells (Bazzi and Anderson, 2014; Garcez et al., 2015; Insolera et al., 2014b; McIntyre
120 et al., 2012). A recent study has shown that the cells of cerebral organoids derived
121 from Cenpj-mutant microcephaly patients present long cilia (Gabriel et al., 2016).
122 Contrary to observations in humans, flies with *Dsas-4* (the ortholog of *Cenpj*)
123 mutations show no cilia or flagella (Basto et al., 2006), and deletion of Cenpj by
124 shRNA treatment blocked cilia formation and caused cilia shortening in CAD (Cath.
125 a-differentiated) cells (Wu and Tang, 2012a). These observations indicate that Cenpj
126 plays a role in NPC proliferation and cilia formation. However, how the balance
127 between centrosome and cilia functions regulates cortical development is largely
128 unknown.

129 By conditionally deleting *Cenpj* in mouse neural progenitor cells, we found longer
130 primary cilia and abnormal cilium appendages in RG cells. The defective cilium
131 disassembly upon Cenpj depletion led to reduced cell proliferation, uncompleted cell
132 division, cell apoptosis, and microcephaly in mice. Cenpj depletion also caused long

133 motile cilia with defective structures in ependymal cells and a reduction in adult
134 neural stem cells in mice. Additionally, we found that Kif2a, a member of the
135 kinesin-13 motor proteins, contributes to Cenpj-regulated cilia disassembly and
136 neurogenesis. These findings indicate that primary cilia dynamics are essential for
137 mitosis of RG cells and are required for constructing a normal cerebral cortex.

138

139

140 Materials and Methods

141 **Animals.** Adult Cenpj^{LacZ} mice (*Cenpj^{tm1a(EUCOMM)Wtsi}*) were obtained from the
142 Welcome Trust Sanger Institute Mouse Genetics Projects (Sanger MGP). Cenpj^{fl/fl}
143 mice were generated by crossing Cenpj^{LacZ} mice with Rosa26^{Flp} mice. Cenpj^{fl/+}
144 Emx1-Cre mice were produced by crossing Cenpj^{fl/fl} mice with Emx1-Cre mice.
145 Cenpj^{CKO} mice were produced by crossing Cenpj^{fl/+} Emx1-Cre mice with Cenpj^{fl/+}
146 Emx1-Cre mice. Cenpj^{CKO}Cilia^{GFP} mice were obtained by cross Cenpj^{fl/+} Emx1-Cre
147 mice with Cilia^{GFP} mice (R26Sstr3GFP, a gift from Dr. Bradley Yoder at the
148 University of Alabama at Birmingham). Animal housing and experimental procedures
149 in this study were in compliance with the guidelines of the Institutional Animal Care
150 and Use Committee of the Institute of Biophysics, Chinese Academy of Sciences. All
151 mice had free access to food and water, were housed in the institutional animal care
152 facility (SPF) with a 12hr light-dark schedule. Both males and females were used for
153 all experiments.

154

155 **Cell culture.** ARPE19 cells were grown in medium containing Dulbecco's modified
156 Eagle's medium (DMEM), 10% (v/v) fetal bovine serum (FBS), 100 U/ml penicillin,
157 100 lg/ml streptomycin (all from Life Technologies GmbH, Darmstadt, Germany),
158 293T cells were grown under standard conditions in DMEM supplemented with 10%
159 FBS. For serum starvation experiments, cells were grown in medium without serum
160 for the described time period and stimulated with 10% FBS-containing medium. Cells
161 were maintained at 37 °C with 5% CO₂.

162

163 **Western blotting.** The tissue and culture cells were lysed in RIPA (added protease
164 inhibitor). Protein samples were separated by SDS-PAGE and transferred to
165 nitrocellulose membranes. After the nitrocellulose membranes were blocked with 5%
166 milk for 1 hour, the nitrocellulose member was incubated with the primary antibody at
167 4 °C overnight and then incubated with horseradish peroxidase-conjugated secondary
168 antibody for 45min at room temperature. Enhanced chemiluminescence reagent
169 (Thermo Scientific) used as western blotting substrate to visualizing the protein bands.

170 The antibodies used as follows: GAPDH (1:5000, KC-5G5, KangChen), Cenpj (1:200,
171 11517-1-AP, Proteintech), Kif2a (1:5000, PAB12407, Abnova).

172

173 **Immunostaining.** Brain slices were fixed in 4% paraformaldehyde in PBS (pH 7.4)
174 and culture cells were fixed in ice-cold methanol, were permeabilized with 0.1%
175 Triton X-100 in PBS for 15 min. and blocked with 10% donkey serum in PBS for 2 h
176 at RT. Antibody incubation were performed overnight at 4 °C for brain slices or 1h at

177 RT for culture cells. Followed by three washes in PBS. Fluorescent-conjugated
178 secondary antibody incubation for 2 h at RT. Images were acquired using a confocal
179 laser scanning microscope (FV1000MPE-BX61W1, Olympus) and were analysed
180 using Fluo View(Olympus), Imaris (Bitplane) and Photoshop (Adobe Systems).
181 Primary antibodies used were as follows: Zo-1(1:300, 339100, Invitrogen), γ -Tubulin
182 (1:5000, T3559, Sigma), γ -Tubulin (1:5000, T5326, Sigma), Acetylated Tubulin
183 (1:30000, T7451, Sigma), Cenpj (1:50, 11517-1-AP, Proteintech), Pericentrin (1:300,
184 611814, BD), GFP (1:500, GFP-1020, Aves), Cleaved Caspase 3 (1:300, 9664, CST),
185 Tbr2 (1:300, ab23345, Abcam), Satb2 (1:300, ab34735, Abcam), Ctip2 (1:300,
186 ab18465, abcam), Ki67 (1:300, ab9260, Millipore), BrdU (1:300, ab6326, Abcam),
187 Pax6 (1:300, PRB-278P, Convance), Sox2 (1:300, sc-17320, Santa Cruz), EdU
188 (Click-iT™ EdU Alexa Fluor™ 594 Imaging Kit, C10339, Thermo), GFAP (1:500,
189 G9269,Sigma), β -Catenin (1:300, 610153, BD). Secondary antibodies used were as
190 follows: donkey anti-mouse, anti-rabbit, anti-chicken, anti-rat or anti-goat Alexa-546-,
191 Alexa-488- and Alexa-647-conjugated antibodies (1:500, Invitrogen). DNA was
192 stained with 49,6-diamidino-2-phenylindole (1:10000, D1306, Invitrogen).
193
194 **Plasmids and *in-utero* electroporation.** Cenpj and Kif2a shRNA sequences were
195 cloned into pLL3.7 vector (addgene #11795) as previously described(Wang et al.,
196 2009). Kif2a sequences were cloned into pEGFP-C1 vector and ptdTomato-C1 vector.
197 Cenpj sequences were cloned into ptdTomato-C1 vector. Electroporation was
198 performed as previously described(Wang et al., 2009). Briefly, timed pregnant CD-1

199 mice (E13.5) were deeply anesthetized with isofluorane, and the uterine horns were
200 exposed through a midline incision. 1 μ l of plasmid DNA (1–2 μ g/ μ l) mixed with Fast
201 Green (Sigma) was manually microinjected into the brain lateral ventricle through the
202 uterus, using a bevelled and calibrated glass micropipette (Drummond Scientific)
203 followed by five 50-ms pulses of 50 mV with a 1s interval delivered across the uterus
204 with two 9-mm electrode paddles positioned on either side of the head (BTX,
205 ECM830).

206

207 **Cortical slice culture and time-lapse imaging.** About 12 h after in utero
208 electroporation, embryos were removed and the brain was extracted into ice-cold
209 artificial cerebrospinal fluid (ACSF) containing (in mM): 125 NaCl, 5 KCl,
210 1.25 NaH₂PO₄, 1 MgSO₄, 2 CaCl₂, 25 NaHCO₃ and 20 Glucose; pH 7.4,
211 310 mOsm l-1. Brains were embedded in 3.5% low-melting agarose in ACSF and
212 sectioned at 300 μ m using a vibratome (Leica Microsystems). Brain slices that
213 contained GFP-expressing cells were transferred on to a slice culture insert (Millicell)
214 in a glass-bottom Petri dish (MatTek Corporation) with culture medium containing
215 (by volume): 66% BME, 25% Hanks, 5% FBS, 1% N-2, 1%
216 penicillin/streptomycin/glutamine (Invitrogen/GIBCO) and 66% D-(+)-glucose
217 (Sigma). Cultures were maintained in a humidified incubator at 37 °C with constant 5%
218 CO₂ supply. two hours later, Petri dishes with slice cultures were transferred to an
219 inverted microscope FV1000 (Olympus). Time-lapse images of dividing radial glia
220 cells were acquired every 10 min for about 5 to 8 h. Images were analysed using Fluo

221 View (Olympus) and Photoshop (Adobe Systems).

222

223 **Real-time PCR assay.** Total RNA was extracted from cells by using SV Total RNA

224 Isolation System (Promega USA). Reverse transcription was performed with Prime

225 ScriptTM II 1st Strand cDNA Synthesis Kit (Takara, Japan), while real-time PCR was

226 performed by using SYBR[®] Premix Ex Taq[™] (Tli RNaseH Plus) (Takara, Japan). The

227 real-time PCR contained: 5 µl of qPCR Mix, 0.4 µl of forward primer, 0.4 µl of

228 reverse primer, 1 µl of cDNA template, and 3.2 µl of ddH₂O. The program: 95 °C for

229 30 s, followed by 40 cycles of 95 °C for 5 s, 60 °C for 10 s, and 72 °C for 15 s. The

230 data were normalized to that of internal control. For primer sequences were in the

231 supplementary information.

232

233 **RNA-seq and library construction.** For RNA-seq analysis, a timed pregnant mouse

234 at E15.5 were anaesthetized. Embryos were removed separately and genotyping was

235 performed to identify the Cenpj^{f/+} and Cenpj^{CKO} pups. Cortical slices of Cenpj^{f/+} and

236 Cenpj^{CKO} embryos were prepared as described above. The VZ/SVZ regions were

237 dissected separately and RNA was isolated using RNeasy Mini kit (Qiagen) according

238 to the manufacturer's instructions. After the samples were tested, the eukaryotic

239 mRNA was enriched by magnetic beads with Oligo (dT); subsequently, using

240 fragmentation buffer to break the mRNA into short fragments; The mRNA was used

241 as a template to synthesize a strand of cDNA with six random bases and then the

242 buffer, dNTPs and DNA polymerase I were used to synthesize the double-stranded

243 cDNA, followed by AMPure XP beads Purified double-stranded cDNA. The purified
244 double-stranded cDNA was subjected to terminal repair, A tail was added and the
245 sequencing adapter was ligated, then the size of the fragment was selected with
246 AMPure XP beads, and finally, PCR-enrichment was performed to obtain the final
247 cDNA library. RNA-seq was performed by Novogene Bioinformatics Institute,
248 Beijing.

249

250 **Scanning electron microscopy.** Mice were anesthetized and perfused with 0.1 M
251 PBS buffer pH 7.4 containing 2.5% glutaraldehyde (Electron Microscopy Sciences)
252 and 2% formaldehyde (Sigma). Brain were then removed and fixed overnight in the
253 same solution at 4 °C and cut into 500 µm thick vibratome sections in PBS, washed
254 three times with PBS, and then dehydrated through an ethanol gradient (30, 60, 90,
255 and 100%). Samples were dried without introducing surface tension artifacts by using
256 critical point drier. After drying, samples were then introduced into the chamber of the
257 sputter coater and coated with a very thin film of gold before SEM examination. 3D
258 reconstruction was analyzed by Amira and Imaris.

259

260 **Transmission electron microscopy.** Mouse embryos were perfused with 2%
261 glutaraldehyde and 2% paraformaldehyde in PBS, then fixed in perfusion solution
262 overnight at 4 °C. The samples were washed three times with PBS then secondarily
263 fixed in 2% osmium tetroxide (Sigma-Aldrich) in cacodylate buffer for 2 h at room
264 temperature. The samples were washed three times with ddH₂O, stained with uranyl

265 acetate then dehydrated through an ethanol gradient (30, 60, 90, and 100%) followed
266 by propylene oxide. Subsequently, samples were embedded in Low Viscosity Resin
267 (TAAB). Sections were cut on a microtome (Leica EM UC6+FC6), and then viewed
268 on a transmission electron microscope (Tecnai Spirit (120 kV)).

269

270 **Three-dimensional model reconstruction.** We took serial images of the brain tissue
271 at 80 nm intervals by focused ion beam scanning electron microscope (FIB-SEM). We
272 manually drew the morphology of the cilium of the ependymal cells in each image,
273 then created a surface using these consecutive pictures by Imaris software. A surface
274 represents a cilium. All of cilia were drawn like this. Multicilia 3D morphology of
275 ependymal cells was reconstructed

276

277 **Quantification of polarity defects.** We employed the algorithm previously published
278 for the characterization of PCP defects in the same system(Boutin et al., 2014). For
279 the analysis of translational polarity defects in EMCCs. Images were imported into
280 MATLAB, saved regions of interest. Cell borders were traced based on Zo-1 label.
281 followed by BB segmentation, based on adaptive thresholding within γ -tubulin
282 channel. Centers of mass were calculated for BBs and cellular outline within every
283 cell. Angles of BBOVs were measured and CSD across all BBOVs within every field
284 of view was assessed. Each experimental condition was characterized by mean and
285 CSDs across all fields of view. CSD values were calculated for BBOV angles. The
286 angles measured within one image plane were normalized by subtracting from their

287 values the average angle of a corresponding field of view, this difference was added to
288 90° and plotted on the summarized graph.

289

290 **Statistical analysis.** All data were represented as the mean ± the SD. Comparisons
291 between two groups were using *t* tests. The quantification of polarity defects used an
292 unpaired Mann–Whitney test. The quantification graphs were analysed by using
293 GraphPad Prism (GraphPad Software). Sample size and *P* values were described in
294 figure legends. Differences were considered significant at *P* < 0.05.

295

296 **Results**

297 **Cenpj deletion in mice causes abnormal cilia and microcephaly**

298 To define the function of Cenpj in ciliogenesis *in vivo* and the cellular basis of
299 centrosome-associated microcephaly, mice with conditional loss-of-function of *Cenpj*
300 (*Cenpj*^{CKO}) were developed by crossing *Cenpj*^{f/f} mice with Emx1-Cre mice, which
301 selectively express Cre recombinase in dorsal telencephalic NPCs (Fig. 1A). Western
302 blot analysis of the mouse cortex lysate at embryonic day 15.5 (E15.5) confirmed that
303 the expression of Cenpj was depleted in the *Cenpj*^{CKO} cortex (Fig. 1B, C). Brain
304 sections were immunostained for Cenpj and Pericentrin, a pericentriolar material
305 protein, and no Cenpj signals were detected in centrosomes on the ventricular surface
306 (VZ) (Fig. 1D). With Cenpj deletion in NPCs of the dorsal telencephalon, the brain
307 hemisphere circumference of *Cenpj*^{CKO} embryos was greatly decreased compared to
308 that of the control *Cenpj*^{+/+} embryos at E15.5 (Fig. 1E, F). Nissl staining of brain

309 slices at E15.5 revealed significantly reduced thickness of the cortex with a normal
310 layered structure upon Cenpj depletion (Fig. 1G, H). We also checked the cortical
311 development of the Cenpj^{+/+} and Cenpj^{CKO} cortex at P7. Although body size was not
312 influenced by Cenpj depletion, a reduced brain size, smaller hemisphere
313 circumference and thinner cortex were observed in the Cenpj^{CKO} mice (Fig. 1I-K).
314 The numbers of early-born Ctip2-expressing deep layer neurons and late-born
315 Statb2-expressing superficial layer neurons were both reduced in the Cenpj^{CKO} cortex
316 (Fig. 1L, M). Consistently, we observed a decrease in Foxp2-expressing layer VI
317 neurons and Cux1-expressing layer II/III neurons following Cenpj depletion but with
318 normal lamination (Fig. 1N-P). The phenotypes were consistent with the phenotypes
319 of microcephaly patients caused by *Cenpj* mutations (Al-Dosari et al., 2010; Gul et al.,
320 2006; Leal et al., 2003); therefore, we used the mouse model to investigate
321 Cenpj-related microcephaly pathogenic mechanisms.
322 To detect the cilia *in vivo*, a Cre recombinase-inducible Cilia^{GFP} mouse(O'Connor
323 et al., 2013) was used. Cenpj^{CKO}Cilia^{GFP} RG cells had longer cilia than
324 Cenpj^{+/+}Cilia^{GFP} RG cells (Fig. 2A, B). As observed by scanning electron microscope,
325 RG cells of the Cenpj^{CKO} mice consistently contained long cilia with a median length
326 of 1.93 ± 0.29 μm compared to RG cells of Cenpj^{+/+} mice, which contained cilia with
327 a median length of 1.11 ± 0.15 μm at E15.5 (Fig. 2C, D). At the end of cortical
328 development, monociliated progenitor cells in the VZ differentiate into multiciliated
329 ependymal cells (Spassky et al., 2005). Hence, a focused ion beam scanning electron
330 microscope (FIB-SEM) was used to capture serial images at 80 nm intervals.

331 Multicilia 3D morphology of ependymal cells was reconstructed (Fig. 2E, Movie 1-4).
332 The reconstructed images showed that the motile cilia length ($11.4 \pm 1.6 \mu\text{m}$) of
333 ependymal cells was increased in $\text{Cenpj}^{\text{CKO}}$ mice compared to that in $\text{Cenpj}^{+/+}$ mice
334 ($7.2 \pm 2.5 \mu\text{m}$) (Fig. 2E, F). In addition, $\text{Cenpj}^{\text{CKO}}$ cilia were disarrayed on the cell
335 surface compared to organized $\text{Cenpj}^{+/+}$ cilia (Fig. 2E). The diameters of the $\text{Cenpj}^{\text{CKO}}$
336 cilia were smaller than those of the $\text{Cenpj}^{+/+}$ cilia (Fig. 2G). Furthermore, on the adult
337 brain ventricle surface of $\text{Cenpj}^{\text{CKO}}$ mice, the motile cilia were curled and tangled
338 with bulges and curly tips when observed by scanning electron microscope (SEM)
339 (Fig. 2H, arrow).

340 Cilia emerge from a tubulin-based structure called the basal body (BB) (Mohan et
341 al., 2013; Yang et al., 2005). Ultrastructural analysis revealed that the majority of
342 primary cilium BBs of $\text{Cenpj}^{\text{CKO}}$ RG cells lacked one or more appendages, including
343 distal appendages (arrowhead) and subdistal appendages (arrow), at E15.5 (Fig. 2I, J).
344 Similarly, the ultrastructure of the motile cilia appendages in adult ependymal cells
345 exhibited abnormal organization upon Cenpj depletion. Unlike the wild-type mice,
346 which had distal and subdistal appendages, the appendages of $\text{Cenpj}^{\text{CKO}}$ mice were
347 hair-like with some parts gathered into a bulging shape. We found approximately 97.9%
348 of RG cells with abnormally disorganized appendages, including distal appendages
349 (arrowhead) and subdistal appendages (arrow), and striated rootlets (asterisks) in the
350 SVZ of adult $\text{Cenpj}^{\text{CKO}}$ mice (Fig. 2K). The aberrant arrangement of the microtubule
351 doublets was also observed in $\text{Cenpj}^{\text{CKO}}$ motile cilia by transmission electron
352 microscopy (TEM) (Fig. 2L, M). Together, these results suggest that Cenpj plays a

353 role in regulating cilia structural elements, including length, width, microtubule
354 structure and appendage organization in embryonic and adult neural progenitor cells.
355
356 **Cenpj controls NPC division by regulating cilia disassembly**
357 It has been demonstrated that ciliary dynamics, including assembly and
358 disassembly, can affect the timing of the cell cycle(Basten and Giles, 2013; Kim and
359 Tsiokas, 2011). Previous research has suggested that primary cilia disassemble when
360 cells enter mitosis in order to release the centrosome to assemble the spindle
361 body(Wang et al., 2014). Consistent with previous observations (Paridaen et al., 2013),
362 we found about 8.2 % RGCs with disassembled cilia by immunostaining of γ -tubulin
363 in the RG cells of Cenpj^{+/+}Cilia^{GFP} mice but this number increased dramatically to
364 33.8% of Cenpj^{CKO}Cilia^{GFP} RG cells at E15.5 (Fig. 3A, B). Consistently, en face
365 views of the VZ showed an increased percentage of prophase and metaphase RG cells
366 and a decreased percentage of anaphase and telophase RG cells on the VZ surface
367 upon Cenpj depletion (Fig. 3C, D). However, Cenpj depletion has no obvious effect
368 on cell-cell adhesion of RG cells as shown by N-cadherin immunofluorescent staining
369 (Fig. 3C). To further observe dividing cells, immunostaining of phosphorylation of
370 histone H3 (PH3) was used to label mitotic RG cells. We observed that more dividing
371 cells were in prophase and metaphase in the Cenpj^{CKO} VZ compared to the Cenpj^{+/+}
372 VZ (Fig. 3E, F), suggesting that the disassembly of cilia blocked the cell cycle of RG
373 cells.
374 Next, we evaluated whether Cenpj depletion delays the mitosis of RG cells. We

375 first reduced Cenpj expression by short-hairpin RNAs (Fig. 3G, H). Cenpj shRNA
376 constructs were electroporated into the mouse cortex via *in utero* electroporation (IUE)
377 at E13.5, and the brains were examined 3 days later (E16.5). In contrast to
378 shControl-GFP-electroporated samples, most of the shCenpj-GFP-transfected cells
379 were found in the intermediate zone (IZ), suggesting that Cenpj depletion impairs
380 neurogenesis, possibly including migration (Fig. 3I, J). This neurogenesis defect was
381 rescued by exogenous expression of Cenpj-td plasmid (Fig. 3K-M). High-efficiency
382 shCenpj-a was selected to be electroporated at E13.5, and cell divisions of RG cells
383 were recorded by timelapse microscopy. Compared to normal interkinetic nuclear
384 migration and mitosis, RG cells stayed in pro/metaphase for an abnormally long time
385 following Cenpj depletion (Fig. 3N and Movie 5, 6). To investigate whether Cenpj
386 regulates cilium disassembly to affect the cell cycle, shCenpj-a transfected ARPE19
387 cells were starved for cilia induction first and then cultured with serum stimulation for
388 24 hours. The ciliated cells were counted 0 hours and 24 hours after serum stimulation.
389 Twenty-four hours after serum stimulation, the deletion of Cenpj led to cilia
390 disassembly delay (Fig. 3O, P) and a significant reduction in the proportion of mitotic
391 cells (Fig. 3Q). Together, our results indicate that abnormal cilia disassembly caused
392 by Cenpj depletion influences RG cell divisions.
393 Since RG cells are mother cells of other types of NPCs involved in cortical
394 development, we next examined how abnormal cilia caused by Cenpj depletion exerts
395 an influence on NPC behavior. NPCs of Cenpj^{+/+} and Cenpj^{CKO} mice at E14.5 were
396 sequentially pulse-chased by using EdU and BrdU, two thymidine analogs, spaced 22

397 hours apart (Fig. 4A). A reduced number of cells with EdU incorporation in Cenpj^{CKO}
398 cortices indicated that fewer cells entered S phase at E14.5 (Fig. 4B). Additionally,
399 66.37 ± 3.13% Cenpj^{+/+} NPCs and 41.32 ± 3.54% Cenpj^{CKO} NPCs in the VZ/SVZ
400 underwent further rounds of cell division in the next 22 hours (Fig. 4C), suggesting
401 that cortical NPCs with Cenpj depletion showed less proliferating potential for
402 consecutive divisions during cortical development. In addition, signals from the
403 apoptosis marker Caspase 3 were observed in the Cenpj^{CKO} cortex at E15.5 (Fig. 4D,
404 E). We next examined the cortical development and neurogenesis capacities of NPCs
405 upon Cenpj depletion. Compared with the control group, decreased expression of the
406 NPC markers Sox2 and Pax6 was observed in the Cenpj^{CKO} cortex compared to the
407 Cenpj^{+/+} cortex at E15.5 (Fig. 4F, G, I). In addition, the population of intermediate
408 progenitor cells (IPCs) identified by Tbr2 was also reduced upon Cenpj depletion (Fig.
409 4F, H). Together, these results suggest that depletion of Cenpj reduces NPC
410 proliferation capacities and progenitor number, resulting in cortical thickness
411 reduction during brain development.

412

413 **Cenpj knockout reduces adult neural stem cells**

414 The conditional Cenpj knockout adult mutants also showed a strong microcephalic
415 phenotype in which the telencephalic area estimated by circumference measurement
416 of Cenpj^{CKO} mice was reduced by 38.0% in 2-month-old mice (Fig. 5A, B). Nissl
417 staining of Cenpj^{+/+} and Cenpj^{CKO} brain slices showed remarkable reductions in the
418 thickness of the cerebral cortex in adult mice upon Cenpj depletion (Fig. 5C, D).

419 Within the ventricular-subventricular zone (V-SVZ) of the adult mammalian brain,
420 adult neural stem cells (aNSCs) remain mitotically active and continuously generate
421 olfactory bulb interneurons (Codega et al., 2014). Glial fibrillary acidic protein
422 (GFAP)-positive B1 cells are considered to be aNSCs (Doetsch et al., 1999; Garcia et
423 al., 2004; Mirzadeh et al., 2008). To examine the aNSCs in the V-SVZ, we visualized
424 the aNSCs and niche astrocytes in the V-SVZ by immunostaining for GFAP. GFAP⁺
425 cells were highly enriched on the surface of the lateral ventricle in Cenpj^{+/+} brains, but
426 only a few GFAP⁺ cells were observed in Cenpj^{CKO} adult brains (Fig. 5E). Consistent
427 with this observation, dramatically reduced Ki67⁺ cells were also observed in the
428 V-SVZ of the Cenpj^{CKO} brains (Fig. 5E). Furthermore, there are fewer SOX2⁺ type C
429 cells in the V-SVZ of the Cenpj^{CKO} brains (Fig. 5F, G). The V-SVZ in the adult
430 mouse brain is a highly organized microenvironment composed of aNSCs and
431 multiciliated ependymal cells, which are responsible for the niche cytoarchitecture
432 and the regulation of the self-renewal and differentiation potential of aNSCs (Gajera
433 et al., 2010; Kuo et al., 2006; Lim et al., 2000; Paez-Gonzalez et al., 2011;
434 Ramirez-Castillejo et al., 2006). En face and side views of the ventricle were labeled
435 by immunofluorescence staining for β-catenin, which is a marker of ependymal cell
436 membranes, and GFAP, which is a marker of B1 cells, in the Cenpj^{+/+}Cilia^{GFP} and
437 Cenpj^{CKO}Cilia^{GFP} brains at P40 (Fig. 5H, I). GFAP⁺ B1 cells were reduced in
438 Cenpj^{CKO} brains, and the orientation of the motile cilia on the ependymal cells was
439 disarrayed in Cenpj^{CKO} brains (Fig. 5H, I). We also found that the lengths of the
440 primary cilia on the B1 cells in Cenpj^{CKO} brains were increased compared to those in

441 Cenpj^{+/+} brains (Fig. 5H, I). Cilia basal bodies (BBs) migrate towards the anterior side
442 of a cell, creating so-called translational polarity, which is critical for the coordinated
443 movement of cilia(Mirzadeh et al., 2010; Wallingford, 2010). We further addressed
444 the BB patches by confocal microscopy using the BB marker γ -tubulin and the
445 ependymal cell membrane marker Zo-1 to reveal the structure of the Cenpj^{+/+} and
446 Cenpj^{CKO} V-SVZ. BB patches are essential for the directional beating of motile cilia.
447 BB patches of Cenpj^{CKO} adult mice often migrated in a different direction from the
448 neighboring cells, while the majority of Cenpj^{+/+} BB patches were in the same
449 direction (Fig. 5J, K). Moreover, adult neural stem cells (aNSCs) continuously
450 generate olfactory bulb interneurons(Codega et al., 2014). Neuron-specific class III
451 β -tubulin (Tuj1) was expressed in immature postmitotic neurons. As expected, Tuj1⁺
452 cells were reduced in the olfactory bulb of Cenpj^{CKO} adult mice compared to those in
453 the olfactory bulb of Cenpj^{+/+} adult mice, especially in the granule cell layer.
454 Moreover, decreased Dcx⁺ cells were also observed in the granule cell layer (Fig. 5L).
455 Taking these results together, we found that Cenpj depletion not only affects aNSC
456 proliferation and adult neurogenesis but also influences the primary cilia of B1 cells
457 and motile cilia of the ependymal cells, showing long cilia with disorganized
458 arrangements.

459
460 **Cenpj regulates cilia disassembly and cortical development through Kif2a**
461 To understand the molecular mechanism underlying how Cenpj depletion leads to
462 cilium abnormality and microcephaly, we performed RNA-Seq to analyze the

463 transcriptome changes in Cenpj-depleted cortices at E15.5. An RNA-Seq correlation
464 test showed the high similarity of the expression patterns between Cenpj^{+/+} and
465 Cenpj^{CKO} samples (Fig. 6A): 11569 genes were expressed in both Cenpj^{CKO} and
466 Cenpj^{+/+} samples, and 1513 genes and 370 genes were expressed in only Cenpj^{+/+} or
467 Cenpj^{CKO} samples, respectively (Fig. 6B). By comparing gene expression levels in
468 Cenpj^{+/+} and Cenpj^{CKO} samples, we found 3517 differentially expressed genes (1643
469 upregulated and 1874 downregulated) (Fig. 6C, log₂(fold change) > 1, q value <
470 0.005). GO term analysis of the downregulated genes in E15.5 Cenpj^{CKO} samples
471 showed a significant enrichment of terms related to cell cycle, cell migration,
472 neurogenesis, neuronal differentiation and axonogenesis, while the upregulated genes
473 were enriched in cell death and cilium assembly (Fig. 6D, E). KEGG signaling
474 pathway analysis revealed that the differentially expressed genes are predicted to be
475 involved in Wnt, MAPK, Hippo, AMPK, and Notch, as well as other signaling
476 pathways (Fig. 6F). With Cenpj depletion, we found that a number of genes involved
477 in cilium disassembly were downregulated in the developing mouse cortex at E15.5,
478 including *Kif2a*, *Kif24*, *Plk1*, *Nek2* and *Ccp110* (Fig. 6G), while some cilium
479 assembly genes were upregulated (Fig. 6H), such as *Rab8a* and *Mks1*, which is
480 consistent with the RNA-Seq data.

481 Cilium assembly and disassembly are tightly controlled by Wnt signaling
482 pathways(Liang et al., 2016; Sanchez and Dynlacht, 2016). Given that Kif2a is a
483 component of the Wnt pathway and plays a role in MT depolymerizing and
484 disassembly of primary cilia(Miyamoto et al., 2015; Trinczek et al., 2004) and that

485 Kif2a transcription was reduced upon Cenpj depletion, we hypothesized that Cenpj
486 may regulate cilia disassembly through the PLK1-Kif2a signaling pathway. To test
487 this hypothesis, we transfected GFP-Kif2a into ARPE19 cells and immunostained
488 with γ -tubulin and anti-Cenpj antibodies. Kif2a was colocalized with Cenpj and
489 γ -tubulin in centrosomes (Fig. 7A). This colocalization of Kif2a and Cenpj also
490 existed when the mother centrioles served as the basal bodies for the primary cilia
491 (Fig. 7B). To examine whether Cenpj regulates cilium disassembly via Kif2a, we first
492 evaluated whether knockdown of Kif2a alone by shRNA disrupted neurogenesis *in*
493 *vivo*. Given that the shRNAs were highly efficient in knocking down Kif2a (Fig. 7C,
494 D), these shRNA constructs were electroporated into the mouse cortex via *in utero*
495 electroporation (IUE) at E13.5, and the brains were examined 3 days later (E16.5).
496 Similar to Cenpj knockdown, Kif2a depletion via two different shRNA plasmids also
497 impaired neurogenesis (Fig. 7E, F). The neurogenesis defects were rescued by
498 expression of the Kif2a-td plasmid (Fig. 7G-I).

499 To analyze whether Kif2a is a downstream effector of Cenpj, thus regulating cilium
500 disassembly, we cotransfected serum-starved ARPE19 cells with control shRNA
501 shKif2a, shCenpj, a combination of shCenpj and GFP-Kif2a, or GFP-Kif2a alone and
502 then cultured the cells with serum stimulation for 24 hours. To evaluate the effect on
503 cilia disassembly, we counted the ciliated cells 0 hours and 24 hours postserum
504 stimulation. We found that deletion of either Cenpj or Kif2a led to a delay in cilia
505 disassembly (Fig. 8A, B). Additionally, the cilia disassembly caused by Cenpj
506 depletion was rescued by expressing Kif2a, while overexpression of Kif2a alone had

507 no effect on cilia disassembly (Fig. 8A, B). We next asked whether Kif2a functions as
508 a downstream effector of Cenpj in regulating cortical neurogenesis. We observed that
509 more neurons migrated to the cortical plate (CP) after Kif2a expression in the shCenpj
510 cortex (Fig. 8C, D). Moreover, Sox2⁺ cells among GFP⁺ Cenpj-knockdown cells were
511 greatly reduced compared to control samples, consistent with the finding that Cenpj
512 depletion reduced the NPC pool in the developing mouse cortex. This Sox2⁺ NPC
513 reduction was rescued by expressing Kif2a (Fig. 8C, E). Together, our results indicate
514 that Kif2a may be a downstream effector facilitating Cenpj to regulate cilium
515 disassembly and is responsible for NPC generation and cortical development.

516

517 **Discussion**

518 In this study, we illustrated the role of Cenpj in regulating cilia disassembly in
519 mouse neural progenitor cells. We found that depletion of Cenpj caused long primary
520 cilia of RG cells at the embryonic stage and long curl motile cilia on ependymal cells
521 at the adult stage. We also demonstrated that Kif2a contributes to Cenpj-controlled
522 primary cilia disassembly, which may be responsible for neural progenitor cell cycle
523 delay and neurogenesis (Fig. 9).

524 So far, microcephaly mutations happen most often in centrosomal proteins.

525 Mutations in *Nde1*, *Cdk5rap2*, *Magoh*, and *Cenpj* induce microcephaly through a
526 combination of loss of progenitor self-renewal, premature differentiation, and
527 progenitor apoptosis(Houlihan and Feng, 2014; Lizarraga et al., 2010; McIntyre et al.,
528 2012; Pawlisz et al., 2008; Silver et al., 2010). The apoptosis induced by *Nde1* and

529 *Cenpj* mutations is p53 dependent(Bazzi and Anderson, 2014; Houlihan and Feng,
530 2014). Overexpressing the centriole duplication protein PLK4 with a microcephaly
531 phenotype is caused by aneuploidy-linked cell death(Marthiens et al., 2013). *Aspm*
532 mutants exhibit mild microcephaly resulting from cell death associated with genomic
533 instability and DNA damage(Fujimori et al., 2014; Williams et al., 2015), whereas
534 *Wdr62* mutant mice have a modestly reduced brain size resulting from premature
535 cell-cycle exit, which causes defects in the mitotic progression of embryonic neural
536 progenitors (Bogoyevitch et al., 2012; Chen et al., 2014). Centrosomes are templates
537 for ciliogenesis, so it is conceivable that altered ciliogenesis could underlie the
538 pathophysiology of microcephaly to some extent. Recent studies have uncovered that
539 the proper timing of cilium disassembly mediated by *Nde1* and *TcTex1* is critically
540 regulated during the cell cycle (Kim et al., 2011; Li et al., 2011; Maskey et al., 2015)
541 and that mutations in *Nde1* cause microcephaly. There have been some studies
542 identifying the role of centrosome proteins in cilium in regulating neural stem cells
543 during cortical development(Breunig et al., 2008; Han et al., 2008; Hu et al., 2014;
544 Willaredt et al., 2008; Wilson et al., 2012). Our results added more information,
545 supporting the idea that ciliogenesis controlled by Cenpj is required for regulation of
546 neural progenitor cell cycles, in addition to its function in cell apoptosis in
547 microcephaly disorders (Gabriel et al., 2016).

548 Cenpj is a conserved centrosomal protein and crucial for centrosome biogenesis and
549 many other important processes besides the cilia-related function. Cenpj regulates
550 centriole duplication(Firat-Karalar and Stearns, 2014; Gonczy, 2012; Hirono, 2014)

551 and elongation(Schmidt et al., 2009). Conditional Cenpj knockout mice show
552 neurogenesis defects and microcephaly due to a loss of centrioles but spindles can still
553 be formed(Insolera et al., 2014a). Cenpj also plays an essential role as a scaffold for
554 cytoplasmic pericentriolar material (PCM) complexes and contributes to the
555 recruitment of PCM to centrioles(Zheng et al., 2014). Dozens of results have shown
556 that Cenpj depletion causes defects in the size of centrosomes at the spindle poles(Cho
557 et al., 2006a; Conduit et al., 2015; Dzhindzhev et al., 2010; Gopalakrishnan et al., 2011;
558 Kirkham et al., 2003; Zheng et al., 2014). Hence, Cenpj mutations or deletions lead to
559 increase of the cells with monopolar, abnormal bipolar, and multipolar spindles,
560 resulting in mitosis arrest and apoptosis(Cho et al., 2006a; Kitagawa et al., 2011b). In
561 addition, cells with abnormal asymmetric bipolar spindles exhibit spindle orientation
562 defects leads to mitotic cleavage randomization(Kitagawa et al., 2011b). The
563 disassembly of cilia affects the natural structure of centrosome and possibly impairs
564 microtubule nucleation capacity, which could also result in spindle disorganization and
565 mispositioning. Hence, our results suggest that neurogenesis failure could be a
566 correlative outcome of the defects in centrosome biogenesis and ciliary disassembly in
567 mice.

568 From the RNA-Seq data, we note that genes in the Wnt signaling pathway, which is
569 important for regulating gene transcription and maintaining microtubule stabilization,
570 were downregulated upon Cenpj depletion, suggesting that related abnormal cilium
571 morphology and dynamics might be regulated via Wnt signals. Indeed, a number of
572 Wnt signaling components have been observed in the axoneme and at the basal bodies,

573 and the noncanonical Wnt signaling pathway has been linked to ciliary assembly
574 (Lienkamp et al., 2012; Wallingford and Mitchell, 2011) and disassembly(Lee et al.,
575 2012). Recent studies, however, have revealed that a mitotic kinase Polo-like kinase 1
576 (Plk1) plays a pivotal role in primary cilia disassembly(Lee et al., 2012;
577 Seeger-Nukpezah et al., 2012; Wang et al., 2013). In response to the ligand Wnt5a,
578 Plk1 forms a complex with Dvl2. The Dvl2-Plk1 complex is required to stabilize and
579 inhibit HEF1 degradation, leading to Aurora A activation, which phosphorylates and
580 activates HDAC6 to increase axonemal microtubule instability, leading to ciliary
581 disassembly(Lee et al., 2012). PLK1 also phosphorylates histone deacetylase 6
582 (HDAC6) to promote tubulin deacetylation and to destabilize the axonemal MTs of
583 primary cilia(Wang et al., 2013). Moreover, PLK1 promotes primary cilia disassembly
584 through the KIF2A pathway via its MT-depolymerizing activity in a growth
585 signal-dependent manner(Miyamoto et al., 2015). Our data support the model that
586 Cenpj-regulated cilia disassembly is due to PLK1-KIF2A pathway dysfunction. *Kif2a*
587 belongs to the *kinesin-13* gene family. Unlike conventional kinesin motor proteins
588 involved in intracellular transport, kinesin-13 proteins do not walk along MTs but
589 have the unique activity of ATP-dependent MT depolymerization(Walczak et al.,
590 2013). Cenpj may recruit Kif2a at the subdistal appendages, which depolymerize
591 centrosomal (cytoplasmic) MT to arrest transport of materials such as tubulin into
592 cilia(Bhogaraju et al., 2013). Further studies are required to clarify how the
593 MT-depolymerizing activity of Kif2a is transmitted to primary cilia disassembly.
594 In most mammals, the V-SVZ continues to produce neurons and glial cells throughout

595 adulthood. Our results indicate a defect in the postnatal stem cell niche of the
596 Cenpj^{CKO} adult mice. The V-SVZ adult neurogenic niche is established at postnatal
597 stages from a subpopulation of embryonic RG cells. RG cells constitute a
598 heterogeneous population of cells that give rise to both type-B1 aNSCs and
599 multiciliated ependymal cells, in addition to neurons and glial cells (Guerout et al.,
600 2014). Depletion of Cenpj in RG cells results in abnormal ciliary structures, such as
601 disorganized basal body structures, long cilia, and misarranged microtubule structures.
602 Similarly, aNSCs and ependymal cells in the SVZ of the Cenpj^{CKO} adult mice also
603 show long cilia and disordered appendages. Depletion of Cenpj not only results in a
604 decrease in embryonic neurogenesis but also influences adult neurogenesis.
605 Ependymal cells and cerebrospinal fluid (CSF) are integral components of the adult
606 V-SVZ niche(Lehtinen et al., 2011), and disruption of motile cilia in ependymal cells
607 is likely to indirectly affect V-SVZ progenitors. As Cenpj depletion also affects the
608 structure of motile cilia in ependymal cells and therefore CSF flow, new approaches
609 to selectively ablate cilia in V-SVZ B1 progenitors, but not ependymal cells, are
610 required to understand the role of primary cilia in these periventricular aNSCs.
611 The primary cilia at the embryonic stage and the adult motile cilia showed similar
612 phenotypes following Cenpj depletion, and motile cilia are terminally differentiated,
613 indicating that there is still an intrinsic pathway controlled by Cenpj interrupted in all
614 cilia independent of the cell cycle. Cenpj is required for centrosome duplication and
615 possesses the ability to destabilize not only cytoplasmic microtubules but also cilium
616 disassembly(Hung et al., 2004; Tang et al., 2009b). A lack of the Cenpj CC5 domain

617 causes long cilia(Gabriel et al., 2016), while the N-terminal tubulin binding domain is
618 responsible for centriole and cilium elongation(Wu and Tang, 2012b). We observed
619 that in addition to cilium length regulation, Cenpj plays roles in controlling the cilium
620 axoneme and basal body structure. The bulging and curly tip phenotype seen
621 following Cenpj depletion may be the result of aberrant arrangement of the
622 microtubule doublets. Individuals with microcephaly have characteristic facies,
623 skeletal dysplasia, and abnormal dentition and have an increased risk of
624 cerebrovascular disease; insulin resistance, severe neonatal cholestasis, and
625 histological dysplasia of the kidneys have also been found in microcephaly
626 patients(Berger et al., 1998; Bober and Jackson, 2017). We speculate that the cilia
627 abnormalities in these organs could be one of the causes of these defects. Our mouse
628 model with *Cenpj* deletion provides an ideal model in which to test this possibility in
629 preclinical studies.

630

631 **References**

- 632 Al-Dosari, M.S., Shaheen, R., Colak, D., and Alkuraya, F.S. (2010). Novel CENPJ mutation causes Seckel
633 syndrome. *J Med Genet* **47**, 411-414.
634 Basten, S.G., and Giles, R.H. (2013). Functional aspects of primary cilia in signaling, cell cycle and
635 tumorigenesis. *Cilia* **2**, 6.
636 Basto, R., Lau, J., Vinogradova, T., Gardiol, A., Woods, C.G., Khodjakov, A., and Raff, J.W. (2006). Flies
637 without centrioles. *Cell* **125**, 1375-1386.
638 Bazzi, H., and Anderson, K.V. (2014). Acentriolar mitosis activates a p53-dependent apoptosis pathway
639 in the mouse embryo. *Proc Natl Acad Sci U S A* **111**, E1491-1500.
640 Berger, A., Haschke, N., Kohlhauser, C., Amman, G., Unterberger, U., and Weninger, M. (1998).
641 Neonatal cholestasis and focal medullary dysplasia of the kidneys in a case of microcephalic
642 osteodysplastic primordial dwarfism. *J Med Genet* **35**, 61-64.
643 Bhogaraju, S., Cajanek, L., Fort, C., Blisnick, T., Weber, K., Taschner, M., Mizuno, N., Lamla, S., Bastin, P.,
644 Nigg, E.A., et al. (2013). Molecular Basis of Tubulin Transport Within the Cilium by IFT74 and IFT81.
645 *Science* **341**, 1009-1012.

-
- 646 Bober, M.B., and Jackson, A.P. (2017). Microcephalic Osteodysplastic Primordial Dwarfism, Type II: a
647 Clinical Review (vol 15, pg 61, 2017). *Curr Osteoporos Rep* 15, 399-399.
- 648 Bogoyevitch, M.A., Yeap, Y.Y.C., Qu, Z.D., Ngoei, K.R., Yip, Y.Y., Zhao, T.T., Heng, J.I., and Ng, D.C.H.
649 (2012). WD40-repeat protein 62 is a JNK-phosphorylated spindle pole protein required for spindle
650 maintenance and timely mitotic progression. *J Cell Sci* 125, 5096-5109.
- 651 Boutin, C., Labedan, P., Dimidschstein, J., Richard, F., Cremer, H., Andre, P., Yang, Y.Z., Montcouquiol,
652 M., Goffinet, A.M., and Tissir, F. (2014). A dual role for planar cell polarity genes in ciliated cells. *P Natl
653 Acad Sci USA* 111, E3129-E3138.
- 654 Breunig, J.J., Sarkisian, M.R., Arellano, J.I., Morozov, Y.M., Ayoub, A.E., Sojitra, S., Wang, B., Flavell, R.A.,
655 Rakic, P., and Town, T. (2008). Primary cilia regulate hippocampal neurogenesis by mediating sonic
656 hedgehog signaling. *P Natl Acad Sci USA* 105, 13127-13132.
- 657 Chen, J.F., Zhang, Y., Wilde, J., Hansen, K.C., Lai, F., and Niswander, L. (2014). Microcephaly disease
658 gene Wdr62 regulates mitotic progression of embryonic neural stem cells and brain size. *Nat Commun*
659 5.
- 660 Cho, J.H., Chang, C.J., Chen, C.Y., and Tang, T.K. (2006a). Depletion of CPAP by RNAi disrupts
661 centrosome integrity and induces multipolar spindles. *Biochem Biophys Res Co* 339, 742-747.
- 662 Cho, J.H., Chang, C.J., Chen, C.Y., and Tang, T.K. (2006b). Depletion of CPAP by RNAi disrupts
663 centrosome integrity and induces multipolar spindles. *Biochem Biophys Res Commun* 339, 742-747.
- 664 Codega, P., Silva-Vargas, V., Paul, A., Maldonado-Soto, A.R., Deleo, A.M., Pastrana, E., and Doetsch, F.
665 (2014). Prospective identification and purification of quiescent adult neural stem cells from their in
666 vivo niche. *Neuron* 82, 545-559.
- 667 Conduit, P.T., Wainman, A., Novak, Z.A., Weil, T.T., and Raff, J.W. (2015). Re-examining the role of
668 Drosophila Sas-4 in centrosome assembly using two-colour-3D-SIM FRAP. *Elife* 4.
- 669 Doetsch, F., Caille, I., Lim, D.A., Garcia-Verdugo, J.M., and Alvarez-Buylla, A. (1999). Subventricular
670 zone astrocytes are neural stem cells in the adult mammalian brain. *Cell* 97, 703-716.
- 671 Dzhindzhev, N.S., Yu, Q.A.D., Weiskopf, K., Tzolovsky, G., Cunha-Ferreira, I., Riparbelli, M.,
672 Rodrigues-Martins, A., Bettencourt-Dias, M., Callaini, G., and Glover, D.M. (2010). Asterless is a
673 scaffold for the onset of centriole assembly. *Nature* 467, 714-U104.
- 674 Firat-Karalar, E.N., and Stearns, T. (2014). The centriole duplication cycle. *Philosophical transactions of
675 the Royal Society of London Series B, Biological sciences* 369.
- 676 Fujimori, A., Itoh, K., Goto, S., Hirakawa, H., Wang, B., Kokubo, T., Kito, S., Tsukamoto, S., and Fushiki, S.
677 (2014). Disruption of Aspm causes microcephaly with abnormal neuronal differentiation. *Brain Dev* 36,
678 661-669.
- 679 Gabriel, E., Wason, A., Ramani, A., Gooi, L.M., Keller, P., Pozniakovsky, A., Poser, I., Noack, F., Telugu,
680 N.S., Calegari, F., et al. (2016). CPAP promotes timely cilium disassembly to maintain neural progenitor
681 pool. *Embo J* 35, 803-819.
- 682 Gajera, C.R., Emich, H., Lioubinski, O., Christ, A., Beckervordersandforth-Bonk, R., Yoshikawa, K.,
683 Bachmann, S., Christensen, E.I., Gotz, M., Kempermann, G., et al. (2010). LRP2 in ependymal cells
684 regulates BMP signaling in the adult neurogenic niche. *J Cell Sci* 123, 1922-1930.
- 685 Garcez, P.P., Diaz-Alonso, J., Crespo-Enriquez, I., Castro, D., Bell, D., and Guillemot, F. (2015).
686 Cenpj/CPAP regulates progenitor divisions and neuronal migration in the cerebral cortex downstream
687 of Ascl1. *Nat Commun* 6, 6474.
- 688 Garcia, A.D., Doan, N.B., Imura, T., Bush, T.G., and Sofroniew, M.V. (2004). GFAP-expressing progenitors
689 are the principal source of constitutive neurogenesis in adult mouse forebrain. *Nat Neurosci* 7,

-
- 690 1233-1241.
- 691 Gonczy, P. (2012). Towards a molecular architecture of centriole assembly. *Nature reviews Molecular*
692 *cell biology* **13**, 425-435.
- 693 Gopalakrishnan, J., Mennella, V., Blachon, S., Zhai, B., Smith, A.H., Megraw, T.L., Nicastro, D., Gygi, S.P.,
694 Agard, D.A., and Avidor-Reiss, T. (2011). Sas-4 provides a scaffold for cytoplasmic complexes and
695 tethers them in a centrosome. *Nat Commun* **2**.
- 696 Guerout, N., Li, X., and Barnabe-Heider, F. (2014). Cell fate control in the developing central nervous
697 system. *Exp Cell Res* **321**, 77-83.
- 698 Gul, A., Hassan, M.J., Hussain, S., Raza, S.I., Chishti, M.S., and Ahmad, W. (2006). A novel deletion
699 mutation in CENPJ gene in a Pakistani family with autosomal recessive primary microcephaly. *J Hum*
700 *Genet* **51**, 760-764.
- 701 Han, Y.G., Spassky, N., Romaguera-Ros, M., Garcia-Verdugo, J.M., Aguilar, A., Schneider-Maunoury, S.,
702 and Alvarez-Buylla, A. (2008). Hedgehog signaling and primary cilia are required for the formation of
703 adult neural stem cells. *Nat Neurosci* **11**, 277-284.
- 704 Hirono, M. (2014). Cartwheel assembly. *Philosophical transactions of the Royal Society of London*
705 *Series B, Biological sciences* **369**.
- 706 Houlihan, S.L., and Feng, Y. (2014). The scaffold protein Nde1 safeguards the brain genome during S
707 phase of early neural progenitor differentiation. *Elife* **3**, e03297.
- 708 Hu, W.F., Pomp, O., Ben-Omran, T., Kodani, A., Henke, K., Mochida, G.H., Yu, T.W., Woodworth, M.B.,
709 Bonnard, C., Raj, G.S., et al. (2014). Katanin p80 Regulates Human Cortical Development by Limiting
710 Centriole and Cilia Number. *Neuron* **84**, 1240-1257.
- 711 Hung, L.Y., Chen, H.L., Chang, C.W., Li, B.R., and Tang, T.K. (2004). Identification of a novel
712 microtubule-destabilizing motif in CPAP that binds to tubulin heterodimers and inhibits microtubule
713 assembly. *Mol Biol Cell* **15**, 2697-2706.
- 714 Insolera, R., Bazzi, H., Shao, W., Anderson, K.V., and Shi, S.H. (2014a). Cortical neurogenesis in the
715 absence of centrioles. *Nat Neurosci* **17**, 1528-1535.
- 716 Insolera, R., Bazzi, H., Shao, W., Anderson, K.V., and Shi, S.H. (2014b). Cortical neurogenesis in the
717 absence of centrioles. *Nat Neurosci* **17**, 1528-1535.
- 718 Kim, S., and Tsikas, L. (2011). Cilia and cell cycle re-entry: more than a coincidence. *Cell Cycle* **10**,
719 2683-2690.
- 720 Kim, S., Zaghloul, N.A., Bubenshchikova, E., Oh, E.C., Rankin, S., Katsanis, N., Obara, T., and Tsikas, L.
721 (2011). Nde1-mediated inhibition of ciliogenesis affects cell cycle re-entry. *Nat Cell Biol* **13**, 351-U350.
- 722 Kirkham, M., Muller-Reichert, T., Oegema, K., Grill, S., and Hyman, A.A. (2003). SAS-4 is a C-elegans
723 centriolar protein that controls centrosome size. *Cell* **112**, 575-587.
- 724 Kitagawa, D., Kohlmaier, G., Keller, D., Strnad, P., Balestra, F.R., Fluckiger, I., and Gonczy, P. (2011a).
725 Spindle positioning in human cells relies on proper centriole formation and on the microcephaly
726 proteins CPAP and STIL. *J Cell Sci* **124**, 3884-3893.
- 727 Kitagawa, D., Kohlmaier, G., Keller, D., Strnad, P., Balestra, F.R., Fluckiger, I., and Gonczy, P. (2011b).
728 Spindle positioning in human cells relies on proper centriole formation and on the microcephaly
729 proteins CPAP and STIL. *J Cell Sci* **124**, 3884-3893.
- 730 Kobayashi, T., and Dynlacht, B.D. (2011). Regulating the transition from centriole to basal body. *J Cell*
731 *Biol* **193**, 435-444.
- 732 Kohlmaier, G., Loncarek, J., Meng, X., McEwen, B.F., Mogensen, M.M., Spektor, A., Dynlacht, B.D.,
733 Khodjakov, A., and Gonczy, P. (2009). Overly long centrioles and defective cell division upon excess of

-
- 734 the SAS-4-related protein CPAP. *Curr Biol* 19, 1012-1018.
- 735 Kuo, C.T., Mirzadeh, Z., Soriano-Navarro, M., Rasin, M., Wang, D., Shen, J., Sestan, N., Garcia-Verdugo,
736 J., Alvarez-Buylla, A., Jan, L.Y., et al. (2006). Postnatal deletion of Numb/Numblike reveals repair and
737 remodeling capacity in the subventricular neurogenic niche. *Cell* 127, 1253-1264.
- 738 Leal, G.F., Roberts, E., Silva, E.O., Costa, S.M., Hampshire, D.J., and Woods, C.G. (2003). A novel locus
739 for autosomal recessive primary microcephaly (MCPH6) maps to 13q12.2. *J Med Genet* 40, 540-542.
- 740 Lee, K.H., Johmura, Y., Yu, L.R., Park, J.E., Gao, Y., Bang, J.K., Zhou, M., Veenstra, T.D., Yeon Kim, B., and
741 Lee, K.S. (2012). Identification of a novel Wnt5a-CK1varepsilon-Dvl2-Plk1-mediated primary cilia
742 disassembly pathway. *Embo J* 31, 3104-3117.
- 743 Lehtinen, M.K., Zappaterra, M.W., Chen, X., Yang, Y.J., Hill, A.D., Lun, M.L., Maynard, T., Gonzalez, D.,
744 Kim, S., Ye, P., et al. (2011). The Cerebrospinal Fluid Provides a Proliferative Niche for Neural
745 Progenitor Cells. *Neuron* 69, 893-905.
- 746 Li, A.Q., Saito, M., Chuang, J.Z., Tseng, Y.Y., Dedesma, C., Tomizawa, K., Kaitsuka, T., and Sung, C.H.
747 (2011). Ciliary transition zone activation of phosphorylated Tctex-1 controls ciliary resorption, S-phase
748 entry and fate of neural progenitors. *Nat Cell Biol* 13, 402-U142.
- 749 Liang, Y., Meng, D., Zhu, B., and Pan, J. (2016). Mechanism of ciliary disassembly. *Cell Mol Life Sci* 73,
750 1787-1802.
- 751 Lienkamp, S., Ganner, A., and Walz, G. (2012). Inversin, Wnt signaling and primary cilia. *Differentiation*
752 83, S49-S55.
- 753 Lim, D.A., Tramontin, A.D., Trevejo, J.M., Herrera, D.G., Garcia-Verdugo, J.M., and Alvarez-Buylla, A.
754 (2000). Noggin antagonizes BMP signaling to create a niche for adult neurogenesis. *Neuron* 28,
755 713-726.
- 756 Lizarraga, S.B., Margossian, S.P., Harris, M.H., Campagna, D.R., Han, A.P., Blevins, S., Mudbhary, R.,
757 Barker, J.E., Walsh, C.A., and Fleming, M.D. (2010). Cdk5rap2 regulates centrosome function and
758 chromosome segregation in neuronal progenitors. *Development* 137, 1907-1917.
- 759 Marthiens, V., Rujano, M.A., Pennetier, C., Tessier, S., Paul-Gilloteaux, P., and Basto, R. (2013).
760 Centrosome amplification causes microcephaly. *Nat Cell Biol* 15, 731-740.
- 761 Maskey, D., Marlin, M.C., Kim, S., Kim, S., Ong, E.C., Li, G.P., and Tsiokas, L. (2015). Cell
762 cycle-dependent ubiquitylation and destruction of NDE1 by CDK5-FBW7 regulates ciliary length. *Embo
763 J* 34, 2424-2440.
- 764 McIntyre, R.E., Lakshminarasimhan Chavali, P., Ismail, O., Carragher, D.M., Sanchez-Andrade, G.,
765 Forment, J.V., Fu, B., Del Castillo Velasco-Herrera, M., Edwards, A., van der Weyden, L., et al. (2012).
766 Disruption of mouse Cenpj, a regulator of centriole biogenesis, phenocopies Seckel syndrome. *Plos
767 Genet* 8, e1003022.
- 768 Mirzadeh, Z., Han, Y.G., Soriano-Navarro, M., Garcia-Verdugo, J.M., and Alvarez-Buylla, A. (2010). Cilia
769 Organize Ependymal Planar Polarity. *J Neurosci* 30, 2600-2610.
- 770 Mirzadeh, Z., Merkle, F.T., Soriano-Navarro, M., Garcia-Verdugo, J.M., and Alvarez-Buylla, A. (2008).
771 Neural stem cells confer unique pinwheel architecture to the ventricular surface in neurogenic regions
772 of the adult brain. *Cell Stem Cell* 3, 265-278.
- 773 Miyamoto, T., Hosoba, K., Ochiai, H., Royba, E., Izumi, H., Sakuma, T., Yamamoto, T., Dynlacht, B.D.,
774 and Matsuura, S. (2015). The Microtubule-Depolymerizing Activity of a Mitotic Kinesin Protein KIF2A
775 Drives Primary Cilia Disassembly Coupled with Cell Proliferation. *Cell Rep* 10, 664-673.
- 776 Mohan, S., Timbers, T.A., Kennedy, J., Blacque, O.E., and Leroux, M.R. (2013). Striated Rootlet and
777 Nonfilamentous Forms of Rootletin Maintain Ciliary Function. *Curr Biol* 23, 2016-2022.

-
- 778 Nigg, E.A., and Stearns, T. (2011). The centrosome cycle: Centriole biogenesis, duplication and
779 inherent asymmetries. *Nat Cell Biol* 13, 1154-1160.
- 780 O'Connor, A.K., Malarkey, E.B., Berbari, N.F., Croyle, M.J., Haycraft, C.J., Bell, P.D., Hohenstein, P.,
781 Kesterson, R.A., and Yoder, B.K. (2013). An inducible CiliaGFP mouse model for in vivo visualization and
782 analysis of cilia in live tissue. *Cilia* 2, 8.
- 783 Paez-Gonzalez, P., Abdi, K., Luciano, D., Liu, Y., Soriano-Navarro, M., Rawlins, E., Bennett, V.,
784 Garcia-Verdugo, J.M., and Kuo, C.T. (2011). Ank3-dependent SVZ niche assembly is required for the
785 continued production of new neurons. *Neuron* 71, 61-75.
- 786 Paridaen, J.T.M.L., Wilsch-Brauninger, M., and Huttner, W.B. (2013). Asymmetric Inheritance of
787 Centrosome-Associated Primary Cilium Membrane Directs Ciliogenesis after Cell Division. *Cell* 155,
788 333-344.
- 789 Pawlisz, A.S., Mutch, C., Wynshaw-Boris, A., Chenn, A., Walsh, C.A., and Feng, Y. (2008).
790 Lis1-Nde1-dependent neuronal fate control determines cerebral cortical size and lamination. *Hum Mol
791 Genet* 17, 2441-2455.
- 792 Pugacheva, E.N., Jablonski, S.A., Hartman, T.R., Henske, E.P., and Golemis, E.A. (2007).
793 HEF1-Dependent aurora a activation induces disassembly of the primary cilium. *Cell* 129, 1351-1363.
- 794 Qin, H.M., Wang, Z.H., Diener, D., and Rosenbaum, J. (2007). Intraflagellar transport protein 27 is a
795 small G protein involved in cell-cycle control. *Curr Biol* 17, 193-202.
- 796 Ramirez-Castillejo, C., Sanchez-Sanchez, F., Andreu-Agullo, C., Ferron, S.R., Aroca-Aguilar, J.D., Sanchez,
797 P., Mira, H., Escribano, J., and Farinas, I. (2006). Pigment epithelium-derived factor is a niche signal for
798 neural stem cell renewal. *Nat Neurosci* 9, 331-339.
- 799 Robert, A., Margall-Ducos, G., Guidotti, J.E., Bregerie, O., Celati, C., Brechot, C., and Desdouets, C.
800 (2007). The intraflagellar transport component IFT88/polaris is a centrosomal protein regulating G1-S
801 transition in non-ciliated cells (vol 120, pg 628, 2006). *J Cell Sci* 120, 918-918.
- 802 Sanchez, I., and Dynlacht, B.D. (2016). Cilium assembly and disassembly. *Nat Cell Biol* 18, 711-717.
- 803 Schmidt, T.I., Kleylein-Sohn, J., Westendorf, J., Le Clech, M., Lavoie, S.B., Stierhof, Y.D., and Nigg, E.A.
804 (2009). Control of centriole length by CPAP and CP110. *Curr Biol* 19, 1005-1011.
- 805 Seeger-Nukpezah, T., Liebau, M.C., Hopker, K., Lamkemeyer, T., Benzing, T., Golemis, E.A., and
806 Schermer, B. (2012). The Centrosomal Kinase Plk1 Localizes to the Transition Zone of Primary Cilia and
807 Induces Phosphorylation of Nephrocystin-1. *Plos One* 7.
- 808 Silver, D.L., Watkins-Chow, D.E., Schreck, K.C., Pierfelice, T.J., Larson, D.M., Burnett, A.J., Liaw, H.J.,
809 Myung, K., Walsh, C.A., Gaiano, N., et al. (2010). The exon junction complex component Magoh
810 controls brain size by regulating neural stem cell division. *Nat Neurosci* 13, 551-558.
- 811 Spassky, N., Merkle, F.T., Flames, N., Tramontin, A.D., Garcia-Verdugo, J.M., and Alvarez-Buylla, A.
812 (2005). Adult ependymal cells are postmitotic and are derived from radial glial cells during
813 embryogenesis. *J Neurosci* 25, 10-18.
- 814 Tang, C.J., Fu, R.H., Wu, K.S., Hsu, W.B., and Tang, T.K. (2009a). CPAP is a cell-cycle regulated protein
815 that controls centriole length. *Nat Cell Biol* 11, 825-831.
- 816 Tang, C.J.C., Fu, R.H., Wu, K.S., Hsu, W.B., and Tang, T.K. (2009b). CPAP is a cell-cycle regulated protein
817 that controls centriole length. *Nat Cell Biol* 11, 825-U103.
- 818 Trinczek, B., Brajenovic, M., Ebneth, A., and Drewes, G. (2004). MARK4 is a novel
819 microtubule-associated proteins/microtubule affinity-regulating kinase that binds to the cellular
820 microtubule network and to centrosomes. *J Biol Chem* 279, 5915-5923.
- 821 Walczak, C.E., Gayek, S., and Ohi, R. (2013). Microtubule-Depolymerizing Kinesins. *Annu Rev Cell Dev*

-
- 822 Bi 29, 417-441.
- 823 Wallingford, J.B. (2010). Planar cell polarity signaling, cilia and polarized ciliary beating. Curr Opin Cell
824 Biol 22, 597-604.
- 825 Wallingford, J.B., and Mitchell, B. (2011). Strange as it may seem: the many links between Wnt
826 signaling, planar cell polarity, and cilia. Gene Dev 25, 201-213.
- 827 Wang, G., Chen, Q., Zhang, X.Y., Zhang, B.Y., Zhuo, X.L., Liu, J.J., Jiang, Q., and Zhang, C.M. (2013).
828 PCM1 recruits Plk1 to the pericentriolar matrix to promote primary cilia disassembly before mitotic
829 entry. J Cell Sci 126, 1355-1365.
- 830 Wang, W., Wu, T., and Kirschner, M.W. (2014). The master cell cycle regulator APC-Cdc20 regulates
831 ciliary length and disassembly of the primary cilium. Elife 3, e03083.
- 832 Wang, X.Q., Tsai, J.W., Imai, J.H., Lian, W.N., Vallee, R.B., and Shi, S.H. (2009). Asymmetric centrosome
833 inheritance maintains neural progenitors in the neocortex. Nature 461, 947-U206.
- 834 Willaredt, M.A., Hasenpusch-Theil, K., Gardner, H.A.R., Kitanovic, I., Hirschfeld-Warneken, V.C., Gojak,
835 C.P., Gorgas, K., Bradford, C.L., Spatz, J., Wolf, S., et al. (2008). A Crucial Role for Primary Cilia in
836 Cortical Morphogenesis. J Neurosci 28, 12887-12900.
- 837 Williams, S.E., Garcia, I., Crowther, A.J., Li, S., Stewart, A., Liu, H., Lough, K.J., O'Neill, S., Veleta, K.,
838 Oyarzabal, E.A., et al. (2015). Aspm sustains postnatal cerebellar neurogenesis and medulloblastoma
839 growth in mice. Development 142, 3921-3932.
- 840 Wilson, S.L., Wilson, J.P., Wang, C.B., Wang, B.L., and McConnell, S.K. (2012). Primary cilia and Gli3
841 activity regulate cerebral cortical size. Dev Neurobiol 72, 1196-1212.
- 842 Wu, K.S., and Tang, T.K. (2012a). CPAP is required for cilia formation in neuronal cells. Biol Open 1,
843 559-565.
- 844 Wu, K.S., and Tang, T.K. (2012b). CPAP is required for cilia formation in neuronal cells. Biol Open 1,
845 559-565.
- 846 Yang, J., Gao, J.G., Adamian, M., Wen, X.H., Pawlyk, B., Zhang, L., Sanderson, M.J., Zuo, J., Makino, C.L.,
847 and Li, T.S. (2005). The ciliary rootlet maintains long-term stability of sensory cilia. Molecular and
848 Cellular Biology 25, 4129-4137.
- 849 Zheng, X.D., Gooi, L.M., Wason, A., Gabriel, E., Mehrjardi, N.Z., Yang, Q., Zhang, X.R., Debec, A., Basiri,
850 M.L., Avidor-Reiss, T., et al. (2014). Conserved TCP domain of Sas-4/CPAP is essential for pericentriolar
851 material tethering during centrosome biogenesis. P Natl Acad Sci USA 111, E354-E363.
- 852
- 853
- 854
- 855
- 856
- 857
- 858
- 859
- 860

861 **Figure Legends**

862 **Figure 1. Cenpj was specifically depleted in the dorsal telencephalon of Cenpj^{CKO}**

863 **mice.**

864 **(A)** A schematic of Cenpj-trapped mice construction strategy. A LacZ reporter
865 cassette and a neo tag, flanked by two FRT sequences, were introduced between
866 the fourth exon and the fifth exon of Cenpj gene locus. The fifth exon were
867 flanked by two LoxP sites in Cenpj^{LacZ} mice. LacZ reporter cassettes can be
868 removed by Flippase splicing, and the Cenpj gene can be knocked out by
869 tissue-specific Cre recombinase splicing.

870 **(B)** Western blot analysis for Cenpj^{+/+} and Cenpj^{CKO} cerebral cortex lysate at E15.5.

871 **(C)** Quantification of Cenpj knockout by western blot. Histogram showing the mean
872 ± SD; ****P < 0.0001 as determined by a t test; n = 3.

873 **(D)** Brain sections were immunostained by anti-Pericentrin (green) antibody and
874 anti-Cenpj (red) antibody on the ventricular surface in Cenpj^{+/+} and Cenpj^{CKO}
875 mice. Scale bar, 10 µm.

876 **(E)** Representative whole mount images of Cenpj^{+/+} and Cenpj^{CKO} brains at E15.5.

877 Scale bar, 0.5 mm.

878 **(F)** Quantification of cerebral hemisphere circumference at E15.5. Data were
879 presented as the mean ± SD; ***P = 0.0004 as determined by a t-test; n = 3.

880 **(G)** Representative images of Cenpj^{+/+} and Cenpj^{CKO} brain coronal sections at E15.5
881 by Nissl staining. Right panel shows magnifying cortical column. Scale bars, 500
882 µm (left) and 100 µm (right).

-
- 883 (H) Histogram of the cerebral cortex thickness. Data were presented as the mean ±
884 SD; **** $P < 0.0001$ as determined by a *t*-test; $n = 3$; 3 brain slices per
885 experiment.
- 886 (I) Body size of Cenpj^{+/+} and Cenpj^{CKO} mice at P7.
- 887 (J) Representative images of the Cenpj^{+/+} and Cenpj^{CKO} brain size at P7. Scale bar, 1
888 mm.
- 889 (K) Quantification of P7 cerebral hemisphere circumference. Data were presented as
890 the mean ± SD; **** $P < 0.0001$ as determined by a *t*-test; $n = 3$.
- 891 (L) Representative images of Ctip2 (green) and Satb2 (red) expressions in the
892 Cenpj^{+/+} and Cenpj^{CKO} cortex at P7, High-magnification images show the cortical
893 column. Scale bar, 30 μ m.
- 894 (M) Quantification of Ctip2⁺ cells and Satb2⁺ cells ratios in the neocortex. Data were
895 presented as the mean ± SD; * $P^{\text{Ctip2}} = 0.0335$, ** $P^{\text{Satb2}} = 0.0011$ as determined by
896 a *t*-test; $n = 3$; 3 brain slices per experiment.
- 897 (N) Representative images of Foxp2 and Cux1 expressions in the Cenpj^{+/+} and
898 Cenpj^{CKO} cortex at P7. Scale bar, 30 μ m.
- 899 (O) Quantification of Foxp2⁺ cells ratios in the neocortex. Data were presented as the
900 mean ± SD; * $P = 0.0175$, as determined by a *t*-test; $n = 3$; 3 brain slices per
901 experiment.
- 902 (P) Quantification of Cux1⁺ cells ratios in the neocortex. Data were presented as the
903 mean ± SD; *** $P = 0.0001$ as determined by a *t*-test; $n = 3$; 3 brain slices per
904 experiment.

-
- 905 **Figure 2. The deletion of the centrosome protein Cenpj causes overly long cilium**
- 906 **and abnormal cilium appendages.**
- 907 **(A)** A model showing how we observed the primary cilium on the endfoot of RG
- 908 cells on the lateral ventricle surface.
- 909 **(B)** Whole-mount immunostaining images showing that Cenpj^{CKO} cilia are longer
- 910 than Cenpj^{+/+} cilia at E15.5. Tight junction protein ZO-1 (red) marks the cell
- 911 membrane of the RG endfoot. Scale bar, 1 μ m.
- 912 **(C)** Scanning electron microscope images of the ventricular surface of Cenpj^{+/+} and
- 913 Cenpj^{CKO} embryo brains at E15.5. Scale bars, 2 μ m (left) and 1 μ m (right).
- 914 **(D)** Quantification of the cilia length in a scatter plot showing the mean \pm SD; ***P
- 915 < 0.0001 as determined by a *t*-test.
- 916 **(E)** Two ways of reconstructing SEM serial sections of the ventricular surface of
- 917 Cenpj^{+/+} and Cenpj^{CKO} adult mouse brain. Scale bar, 2 μ m.
- 918 **(F)** Quantification of the cilia length in a scatter plot showing the mean \pm SD; ***P
- 919 < 0.0001 as determined by a *t*-test.
- 920 **(G)** Quantification of the cilia width in a scatter plot showing the mean \pm SD; ***P
- 921 < 0.0001 as determined by a *t*-test.
- 922 **(H)** SEM images of the Cenpj^{+/+} and Cenpj^{CKO} adult brain ventricular surface. The
- 923 motile cilia are magnified. Arrow shows the cilia tip. Scale bars, 10 μ m (left and
- 924 right top) and 1 μ m (right bottom).
- 925 **(I)** Transmission electron microscope images of Cenpj^{+/+} and Cenpj^{CKO} cilium
- 926 appendages of RG at E15.5. Distal appendages (arrowhead) and subdistal

927 appendages (arrow) in Cenpj^{+/+} and Cenpj^{CKO} basal bodies. Scale bar, 250 nm.

928 (J) The percentages of normal and abnormal cilium in Cenpj^{+/+} and Cenpj^{CKO} mouse
929 embryo RG cells.

930 (K) Transmission electron microscope images of Cenpj^{+/+} and Cenpj^{CKO} adult cilia
931 appendages. Normal distal appendages (arrowhead) and subdistal appendages
932 (arrow) in Cenpj^{+/+} cilia. Asterisk shows striated rootlets. Scale bar, 100 nm.

933 (L) Transmission electron microscope images of Cenpj^{+/+} and Cenpj^{CKO} adult cilia
934 microtubule arrangement. The Cenpj^{CKO} mouse displays disorganized
935 microtubule doublets (blue dots). Scale bar, 100 nm.

936 (M) Quantification of the percentages of normal and abnormal Cenpj^{+/+} or Cenpj^{CKO}
937 adult cilia microtubule arrangement.

938

939 **Figure 3. Cenpj regulates cilia disassembly and RG division.**

940 (A) Representative images of the mitotic cells on the lateral ventricle surface of
941 Cenpj^{+/+} Cilia^{GFP} and Cenpj^{CKO} Cilia^{GFP} embryo brains. Cilia (green), γ -tubulin
942 (red). Scale bar, 10 μ m.

943 (B) Quantification of the mitotic cells with cilia in pro/metaphase versus in
944 ana/telophase on the Cenpj^{+/+} and Cenpj^{CKO} mouse lateral ventricle surface.
945 Histogram showing the mean \pm SD; $****P^{\text{pro/metaphase}} < 0.0001$, $****P^{\text{ana/telophase}} <$
946 0.0001 as determined by *t*-test; $n = 3$; >200 cells per experiment.

947 (C) En face views of the embryo ventricular zone in Cenpj^{+/+} and Cenpj^{CKO} mice
948 stained for N-Cadherin (green) and DAPI (blue). High magnification images

949 indicate cell adhesion. Arrowheads indicated the mitotic cells. Scale bar, 10 μ m.

950 **(D)** Quantification of the mitotic cells in pro/metaphase versus those in ana/telophase
951 on the Cenpj^{+/+} and Cenpj^{CKO} mouse lateral ventricle surface. Histogram showing
952 the mean \pm SD; * P ^{pro/metaphase} = 0.0230, * P ^{ana/telophase} = 0.0230 as determined by
953 *t*-test; $n=3$; 3 brain slices per experiment.

954 **(E)** Representative images of mitotic cells at the VZ surface in E13.5 Cenpj^{+/+} or
955 Cenpj^{CKO} cortices stained for PH3 (red) and DAPI (blue). High magnification
956 images indicate mitotic cells. Scale bar, 10 μ m.

957 **(F)** Quantification of the fraction of mitotic cells in pro/metaphase (white) versus
958 those in ana/telophase (black), which reflects mitotic progression. Histogram
959 showing the means \pm SD; ** P ^{pro/metaphase} = 0.0037, ** P ^{ana/telophase} = 0.0037 as
960 determined by *t* test; $n = 3$; >200 cells per experiment.

961 **(G)** Cenpj was efficiently knocked down by Cenpj shRNAs. GAPDH serving as a
962 loading control.

963 **(H)** Quantification of Cenpj knockdown efficiency by shRNAs. Histograms showing
964 the mean \pm SD; **** P ^{shCtrl vs. shCenpj-a} < 0.0001, as determined by *t*-test; $n=3$.

965 **(I)** Analysis of the radial migration of cortices 3 days after in utero electroporation at
966 E13.5. Scale bar, 30 μ m.

967 **(J)** Quantification of the neurogenesis after silencing Cenpj by measuring the
968 percentages of GFP⁺ cells that have reached different zones of the cortex 3 days
969 after electroporation. Histograms showing the mean \pm SD; shCtrl vs. shCenpj-a
970 (**** P ^{CP} < 0.0001, *** P ^{I_Z} = 0.0008, *** P ^{V_Z/S_{V_Z}} = 0.0004 as determined by a

971 *t*-test; $n = 3$; 9 brain slices per experiment).

972 **(K)** Cenpj was specifically knocked down by shCenpj-a and was rescued by the
973 overexpression of Cenpj-td plasmid. GAPDH serving as a loading control.

974 **(L)** Quantification of Cenpj protein expression index. Histograms showing the mean
975 \pm SD; $****P$ shCtrl+RFP vs. shCenpj-a+RFP < 0.0001 as determined by a *t*-test; $n=3$.

976 **(M)** Analysis of the radial migration of cortices 3 days after in utero electroporation at
977 E13.5. Scale bar, 30 μ m.

978 **(N)** Representative time-lapse images of the RG dividing process in the sections of
979 the cerebral cortex electroporated with shCtrl and shCenpj in the wild-type mouse.
980 Arrowheads indicate mother RG cells, and asterisks indicate two daughter cells.
981 Scale bar, 20 μ m.

982 **(O)** Ciliogenesis in ARPE19 cells. Cells were treated, fixed at 0 h or at 24 h after
983 serum restimulation, and were immunostained with anti- γ -tubulin (red) and
984 anti-acetylated tubulin (gray) antibodies. Enlarged views show the centrosome
985 (right top) and the primary cilia (right bottom). Arrows indicate the cilia. Scale
986 bar, 10 μ m.

987 **(P)** The percentage of ARPE19 cells with primary cilia in GFP-positive cells.
988 Histogram showing the means \pm SD; $P^{0\text{hr}} = 0.7091$, $*P^{24\text{hr}} = 0.0109$ as
989 determined by a *t*-test; $n > 200$ cells.

990 **(Q)** Quantification of the fraction of mitotic cells in pro/metaphase versus those in
991 ana/telophase. Histogram showing the means \pm SD; *t* test; $P^{0\text{hr,pro/metaphase}} =$
992 0.9106, $P^{0\text{hr,ana/telophase}} = 0.4686$, $****P^{24\text{hr,pro/metaphase}} < 0.0001$, $****P^{24\text{hr}}$,

993 ana/telophase < 0.0001 as determined by a *t*-test; *n* > 200 cells.

994 **Figure 4. Cenpj deletion in the cortex influences RG cell proliferation during**
995 **development.**

- 996 **(A)** Representative images of E15.5 Cenpj^{+/+} and Cenpj^{CKO} cortices subjected to dual
997 pulse-chase labeling of EdU (red) and BrdU (green). The pulse-chase timing is
998 shown on the top. High-magnification images showing the cortical column and
999 NPCs in the VZ/SVZ. Arrowheads indicate BrdU (green)-positive cells and
1000 arrows indicate BrdU (green) and EdU (red) double-positive cells. Scale bars, 100
1001 μm (top), 10 μm (left), and 30 μm (right).
- 1002 **(B)** Quantification of EdU (red) incorporation in the Cenpj^{+/+} and Cenpj^{CKO} VZ/SVZ
1003 after 24 h. Histogram showing the mean ± SD; *****P* < 0.0001 as determined by
1004 *t*-test; *n* = 3; 3 brain slices per experiment.
- 1005 **(C)** Quantification of EdU (red) and BrdU (green) double incorporation in Cenpj^{+/+}
1006 and Cenpj^{CKO} mouse VZ/SVZ. Histogram showing the mean ± SD; ****P* =
1007 0.0008 as determined by *t*-test; *n* = 3; 3 brain slices per experiment.
- 1008 **(D)** Representative images of Caspase3 staining in Cenpj^{+/+} and Cenpj^{CKO} brain at
1009 E15.5. Right panel shows magnifying cortical column. Scale bars, 30 μm (left)
1010 and 100 μm (right).
- 1011 **(E)** Quantification of Caspase3⁺ (green) cells in the cortex. Histogram showing the
1012 mean ± SD; ***P* = 0.0044 as determined by *t*-test; *n* = 3; 3 brain slices per
1013 experiment.
- 1014 **(F)** Neural progenitors are reduced in the Cenpj^{CKO} cortex. Representative images of

1015 Cenpj^{+/+} and Cenpj^{CKO} cortices at E15.5, which were stained with antibodies
1016 against Sox2 (red), Tbr2 (green), and Pax6 (red).

1017 **(G)** Quantification of Sox2⁺ cell ratios in the VZ/SVZ. Histogram showing the mean
1018 ± SD; **P = 0.0031 as determined by *t*-test; n = 3; 3 brain slices per experiment.

1019 **(H)** Quantification of Tbr2⁺ cell ratios in the VZ/SVZ. Histogram showing the mean ±
1020 SD; ****P < 0.0001 as determined by *t*-test; n = 3; 3 brain slices per experiment.

1021 **(I)** Quantification of Pax6⁺ cell ratios in the VZ/SVZ. Histogram showing the mean ±
1022 SD; ****P < 0.0001 as determined by *t*-test; n = 3; 3 brain slices per experiment.

1023

1024 **Figure 5. Cenpj knockout results in defective brains in adult mice.**

1025 **(A)** Representative images of the Cenpj^{+/+} and Cenpj^{CKO} brain size at adult. Cenpj^{CKO}
1026 mice show severe microcephaly. Scale bar, 5 mm.

1027 **(B)** Quantification of the mouse cerebral hemisphere circumference, Histogram
1028 showing the mean ± SD; ****P < 0.0001 as determined by a *t*-test; n = 3.

1029 **(C)** Representative images of Cenpj^{+/+} and Cenpj^{CKO} brain cortical column at 2
1030 months by Nissl staining. Right panel shows magnifying. Scale bar, 100 µm.

1031 **(D)** Histogram of the cortical thickness between the Cenpj^{+/+} and Cenpj^{CKO} adult
1032 cerebral cortex. Data are shown as the means ± SD; ****P < 0.0001 as
1033 determined by a *t*-test; n = 3; 3 brains per experiment.

1034 **(E)** Representative images of Cenpj^{+/+} and Cenpj^{CKO} brain slices stained with GFAP
1035 (green). The right panel shows the magnified lateral ventricles stained with GFAP
1036 (green) and Ki67 (red). Scale bars, 500 µm (left top) and 200 µm (left bottom and

1037 right).

1038 **(F)** Representative images of Cenpj^{+/+} and Cenpj^{CKO} brain slices stained with Sox2
1039 (red). Scale bars, 60 μ m.

1040 **(G)** Quantification of Sox2⁺ cell ratios in the V-SVZ. Histogram showing the mean \pm
1041 SD; ***P < 0.0001 as determined by *t*-test; n = 3; 3 brain slices per experiment.

1042 **(H)** Whole-mount ventricles of Cenpj^{+/+} and Cenpj^{CKO} brains at postnatal day 40
1043 (P40), which were stained with antibodies against GFAP (gray) and β -catenin (red)
1044 in the Cenpj^{+/+}Cilia^{GFP} and Cenpj^{CKO}Cilia^{GFP} mouse V-SVZ. Scale bar, 30 μ m
1045 (left) and 10 μ m (right).

1046 **(I)** En face views of the adult subventricular zone pinwheel structure in
1047 Cenpj^{+/+}Cilia^{GFP} and Cenpj^{CKO}Cilia^{GFP} brains at P40. Scale bar, 60 μ m.

1048 **(J)** Basal body (BB) polarization in ependymal multiciliated cells. The left panel
1049 shows tissue polarization in the Cenpj^{+/+} and Cenpj^{CKO} mice. Right panels
1050 illustrate the algorithm for quantification of translational polarity. Scale bar, 10
1051 μ m.

1052 **(K)** Quantification of basal body translational polarity. The angles for basal body
1053 orientation vectors (BBOVs) were calculated, and angular histogram plots are
1054 shown (on average 20 cells per field of view were analyzed). P<0.0001 as
1055 determined by an unpaired Mann–Whitney test.

1056 **(L)** Representative images of Cenpj^{+/+} and Cenpj^{CKO} olfactory bulb coronal sections
1057 stained with antibodies specific to Tuj1 (red) and Dcx (green). Right panels show
1058 the magnified images. Scale bars, 200 μ m (left) and 100 μ m (right).

1059

1060 **Figure 6. Transcriptome changes in the developing mouse cortex with Cenpj
1061 depletion.**

1062 **(A)** RNA-Seq correlation of the gene expression level.

1063 **(B)** Venn diagrams of the co-expression genes between Cenpj^{CKO} samples and
1064 Cenpj^{+/+} samples.

1065 **(C)** Scatter plot analysis of transcriptom expression profiles of Cenpj^{CKO} samples
1066 versus Cenpj^{+/+} samples at E15.5. Red dots and green dots highlight the

1067 significantly upregulated or downregulated expressed genes after Cenpj depletion.

1068 Blue dots show no significantly changed genes.

1069 **(D)** Histogram of the enriched GO terms of downregulated genes from the pairwise
1070 comparison of Cenpj^{CKO} versus Cenpj^{+/+}. The significance of each GO term was
1071 estimated based on corrected *P* values (corrected *P* < 0.05).

1072 **(E)** Histogram of the enriched GO terms of upregulated genes from the pairwise
1073 comparison of Cenpj^{CKO} versus Cenpj^{+/+}. The significance of each GO term was
1074 estimated based on corrected *P* values (corrected *P* < 0.05).

1075 **(F)** Statistics of enriched KEGG pathway display the varying genes that are involved
1076 in many pathways. The size of the point indicates the number of differentially
1077 expressed genes in this pathway, and the color of the points corresponds to a
1078 different *q*-value range.

1079 **(G)** Quantitative real-time PCR-analyzed transcription of genes involved in cilium
1080 disassembly. All measured values were normalized to GAPDH gene expression.

1081 Histogram showing the mean ± SD; *** $P^{\text{Cenpj}} = 0.0008$, *** $P^{\text{Kif2a}} = 0.0002$, * P
1082 $\text{Kif24} = 0.0220$, *** $P^{\text{Plk1}} = 0.0002$, ** $P^{\text{Nek2}} = 0.0056$, *** $P^{\text{Ccp110}} = 0.0005$, P^{Cep97}
1083 = 0.1788 as determined by *t*-test; $n = 3$; 3 repetitions per experiment.

1084 (H) Quantitative real-time PCR-analyzed transcription of genes involved in cilium
1085 assembly. All measured values were normalized to GAPDH gene expression.
1086 Histogram showing the mean ± SD; * $P^{\text{Rab8a}} = 0.0484$, $P^{\text{Odf2}} = 0.3714$, $P^{\text{Sctl1}} =$
1087 0.3873, ** $P^{\text{Mks1}} = 0.0038$, $P^{\text{Cep89}} = 0.7596$, ** $P^{\text{Fbf1}} = 0.0060$ as determined by
1088 *t*-test; $n = 3$; 3 repetitions per experiment.

1089

1090 **Figure 7. Cenpj regulates cortical development via Kif2a.**

1091 (A) ARPE19 cells were Immunostained with anti- γ -tubulin (gray) and anti-Cenpj (red)
1092 antibodies. Scale bars, 2 μm .

1093 (B) ARPE19 cells were transfected with GFP-Kif2a and immunostained with anti-
1094 acetylated tubulin (gray) and anti-Cenpj (red) antibodies. An arrow indicates the
1095 cilium. Scale bar, 10 μm .

1096 (C) Overexpressed Kif2a was efficiently knocked down by Kif2a shRNAs. GAPDH
1097 serving as a loading control.

1098 (D) Quantification of Kif2a knockdown efficiency by shRNAs. Histograms showing
1099 the mean ± SD; *** $P^{\text{shCtrl vs. shKif2a-1}} < 0.0001$, *** $P^{\text{shCtrl vs. shKif2a-2}} < 0.0001$ as
1100 determined by a *t*-test; $n=3$.

1101 (E) Analysis of the radial migration of cortices 3 days after *in utero*
1102 co-electroporation at E13.5 with control shRNA, shKif2a-1, shKif2a-2. Scale bar,

1103 30 μ m.

1104 (F) Quantification of the neurogenesis after silencing Kif2a by measuring the
1105 percentages of GFP⁺ cells that have reached the different zones of the cortex 3
1106 days after electroporation. Histograms showing the mean \pm SD; shCtrl vs.
1107 shKif2a-2 ($****P^{CP} < 0.0001$, $**P^{IZ} = 0.0025$, $****P^{VZ/SVZ} < 0.0001$ as
1108 determined by a *t*-test; $n = 3$; 9 brain slices per experiment).

1109 (G) Kif2a are specifically knocked down by shKif2a-2 and rescued by overexpression
1110 of Kif2a-td plasmid. GAPDH serving as a loading control.

1111 (H) Quantification of Kif2a protein expression index. Histograms showing the mean
1112 \pm SD; $****P^{shCtrl+RFP \text{ vs. } shKif2a-2+RFP} < 0.0001$ as determined by a *t*-test; $n=3$.

1113 (I) Analysis of the radial migration of cortices 3 days after in utero electroporation at
1114 E13.5. Scale bar, 30 μ m.

1115

1116 **Figure 8. Kif2a rescues the phenotype caused by Cenpj deletion.**

1117 (A) Ciliogenesis in ARPE19 cells. Cells were treated, fixed at 0 h or at 24 h after
1118 serum restimulation, and were immunostained with anti- γ -tubulin (purple) and
1119 anti-acetylated tubulin (red) antibodies. Enlarged views show the centrosome
1120 (right top) and primary cilia (right bottom). Arrows indicate the primary cilia.
1121 Scale bar, 10 μ m.

1122 (B) The percentage of ARPE19 cells with primary cilia in GFP-positive cells.
1123 Histogram showing the means \pm SD; $*P^{24\text{hr}, \text{Ctrl vs. Cenpj-KO}} = 0.0151$, $*P^{24\text{hr}, \text{Ctrl vs.}}$
1124 Kif2a-KO} = 0.0129, $P^{24\text{hr}, \text{Ctrl vs. Cenpj-KO+Kif2a}} = 0.4584$, $P^{24\text{hr}, \text{Ctrl vs. Kif2a-OX}} = 0.1250$,

1125 * $P^{24\text{hr}, \text{Kif2a-KO vs. Cenpj-KO+Kif2a}} = 0.0475$, * $P^{24\text{hr}, \text{Kif2a-KO vs Kif2a-OX}} = 0.0424$ as
1126 determined by a *t* test; $n = 3$; >200 cells per experiment.

1127 **(C)** Neurogenesis defects caused by Cenpj depletion were rescued by Kif2a
1128 expression. Confocal images of cortices 3 days after in utero coelectroporation at
1129 E13.5. shRNA-GFP (green), Kif2a-RFP (red), Sox2 (gray). Scale bar, 30 μm .

1130 **(D)** Quantification of the migration of neurons by measuring the percentages of GFP⁺
1131 and RFP⁺ cells that reached the different zones of the cortex 3 days after
1132 electroporation. Histogram showing the means \pm SD; shCtrl+RFP vs.
1133 shCenpj+RFP ($****P^{\text{CP}} < 0.0001$, $****P^{\text{IZ}} < 0.0001$, $****P^{\text{SVZ}} < 0.0001$, $**P$
1134 $^{\text{VZ}} = 0.0039$ as determined by a *t*-test; $n = 3$; 9 brain slices per experiment).

1135 **(E)** Quantification of the neural stem cell number was measured by counting the
1136 percentage of GFP⁺RFP⁺Sox2⁺ cells in the VZ/SVZ. Histogram showing the
1137 means \pm SD; $***P^{\text{shCtrl+RFP vs. shCenpj+RFP}} = 0.0008$, $P^{\text{shCtrl+RFP vs. shCenpj+Kif2a}} =$
1138 0.5416 , $P^{\text{shCtrl+RFP vs. shCtrl+Kif2a}} = 0.8628$, $**P^{\text{shCenpj+RFP vs. shCenpj+Kif2a}} = 0.0011$, *t*
1139 test; $n = 3$; 9 brain slices per experiment.

1140

1141 **Figure 9. The model of Cenpj function in neurogenesis in the developing**
1142 **neocortex.** Depletion of Cenpj causes long primary cilia and abnormal appendages of
1143 RG cells at the embryonic stage, resulting in neural progenitor cell cycle blockage and
1144 cell death. At the adult stage, depletion of Cenpj contributes to long thin motile cilia
1145 with curly tips on the ependymal cells and long primary cilia on the B cells. Abnormal
1146 arrangement of the microtubule doublets and disorganized cilia appendages were also

1147 observed. We illustrate that Cenpj regulates cilia disassembly and neurogenesis
1148 through Kif2a.

1149

1150 **Movie 1 (related to Figure 2E).** 3D reconstruction of the ependymal cell multicilia
1151 morphology of the Cenpj^{+/+} adult mouse brain by Amira, composed of 143 images
1152 with 80 nm intervals. The scale bar is 2 μ m.

1153

1154 **Movie 2 (related to Figure 2E).** 3D reconstruction of the ependymal cell multicilia
1155 morphology of the Cenpj^{CKO} adult mouse brain by Amira, composed of 131 images
1156 with 80 nm intervals. The scale bar is 2 μ m.

1157

1158 **Movie 3 (related to Figure 2E).** 3D reconstruction of the ependymal cell multicilia
1159 morphology of the Cenpj^{+/+} adult mouse brain by Imaris, composed of 143 images
1160 with 80 nm intervals. The scale bar is 2 μ m.

1161

1162 **Movie 4 (related to Figure 2E).** 3D reconstruction of the ependymal cell multicilia
1163 morphology of the Cenpj^{CKO} adult mouse brain by Imaris, composed of 131 images
1164 with 80 nm intervals. The scale bar is 2 μ m.

1165

1166 **Movie 5 (related to Figure 3N).** Representative time-lapse movie of the RGC
1167 dividing process in the sections of the cerebral cortex electroporated with shCtrl in the
1168 wild type mouse.

1169

1170 **Movie 6 (related to Figure 3N).** Representative time-lapse movie of the RGC
1171 dividing process in the sections of the cerebral cortex electroporated with shCenpj in
1172 the wild type mouse.

1173

1174

1175

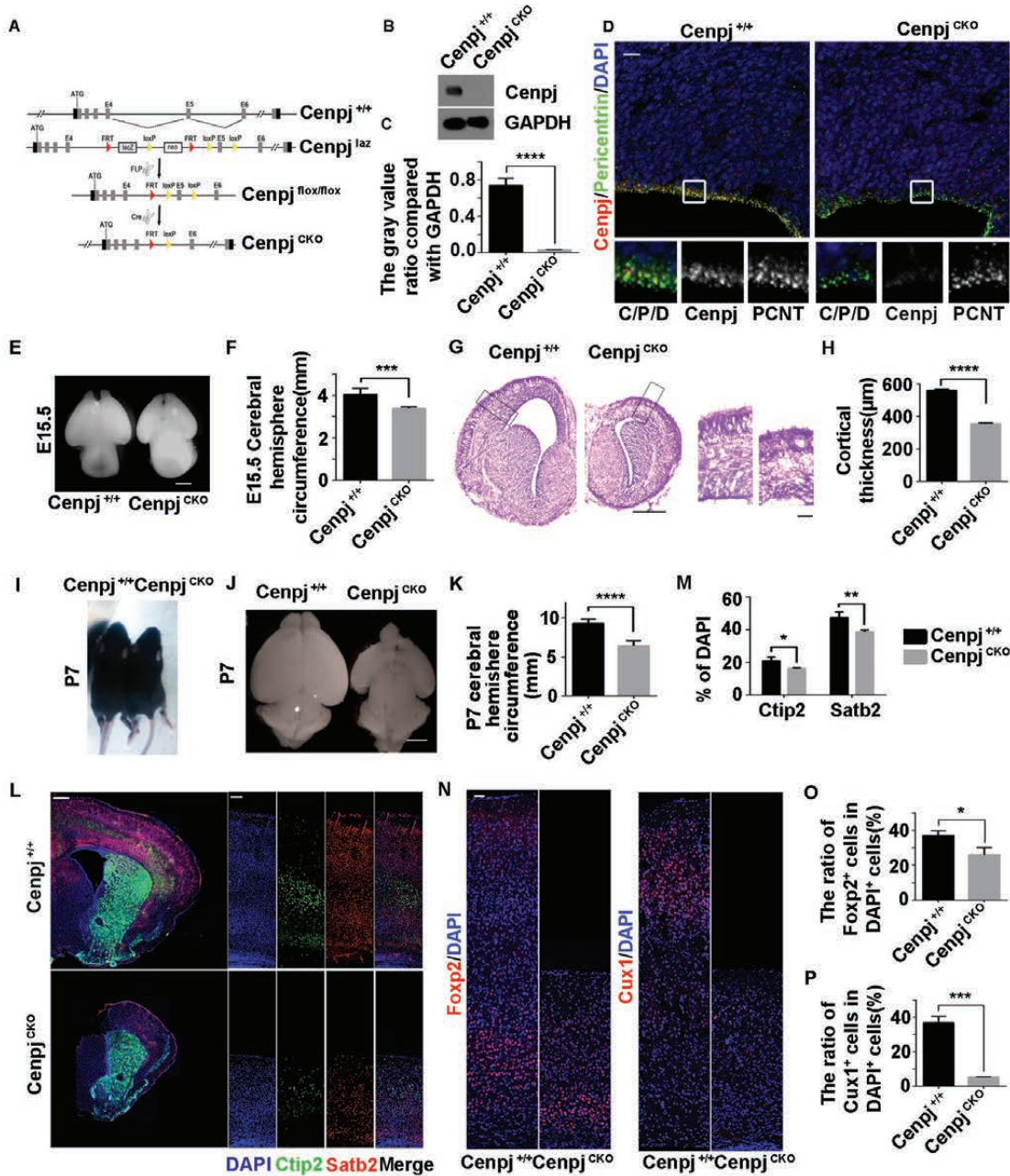


Figure 1

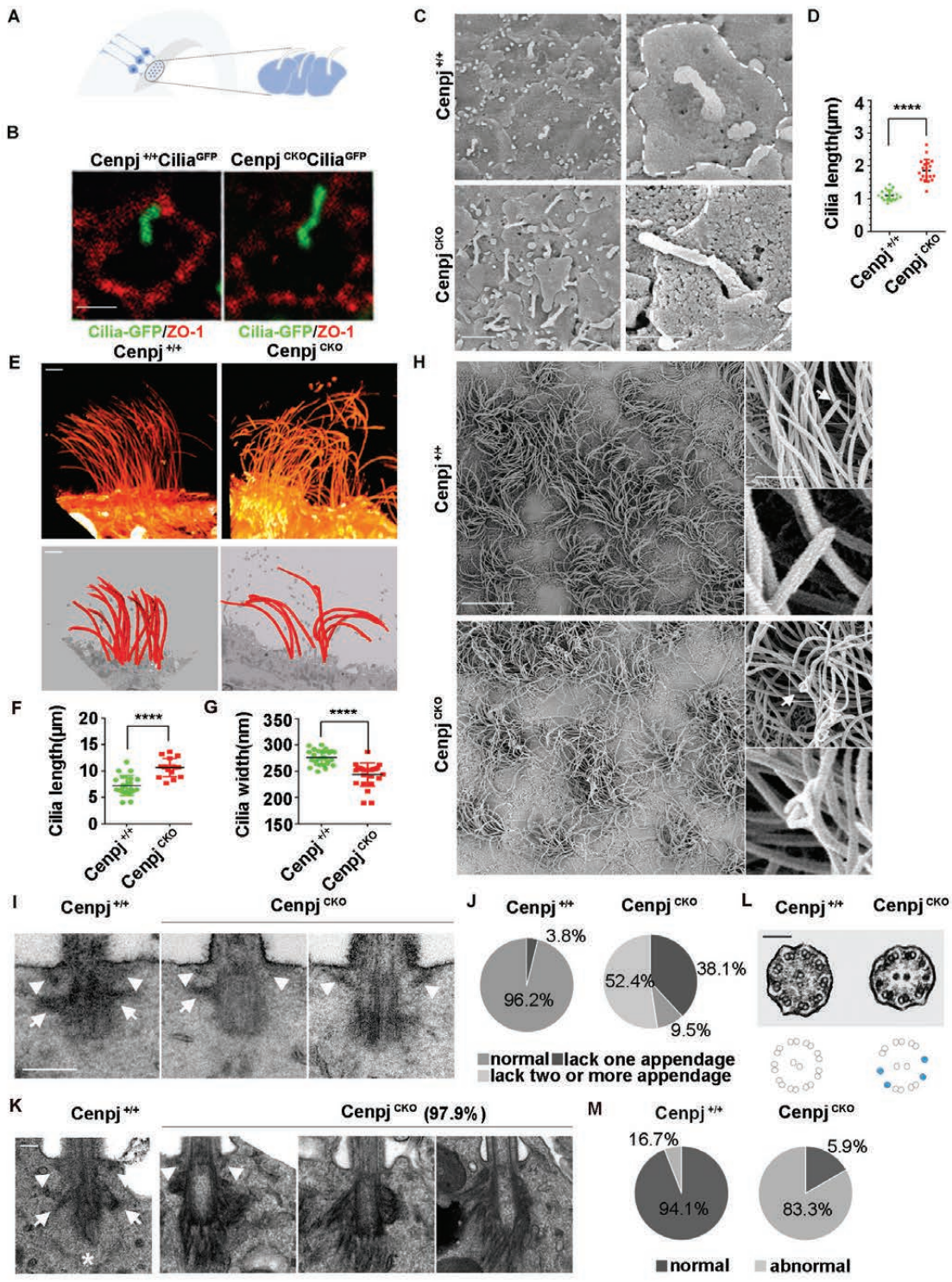


Figure 2

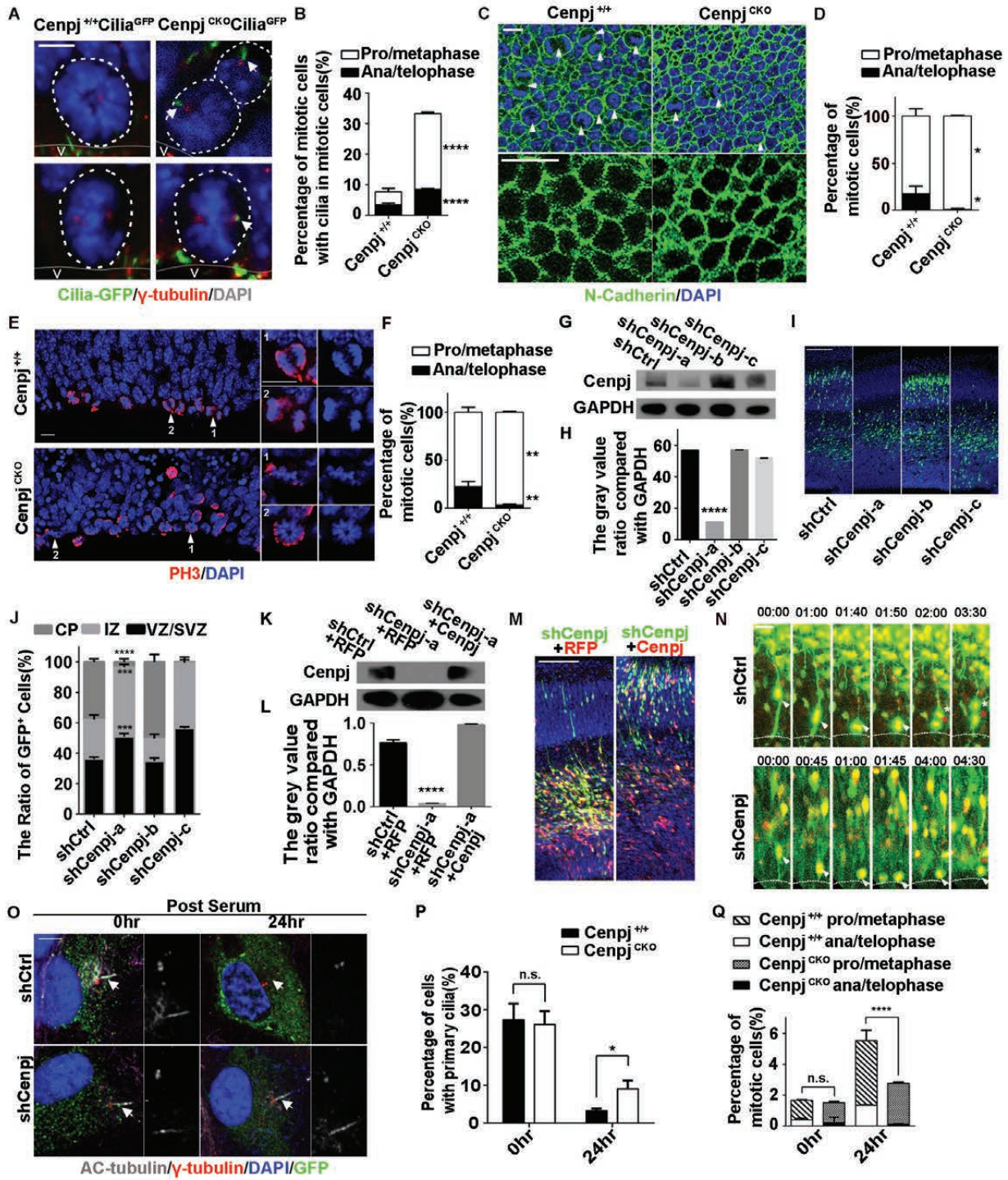


Figure 3

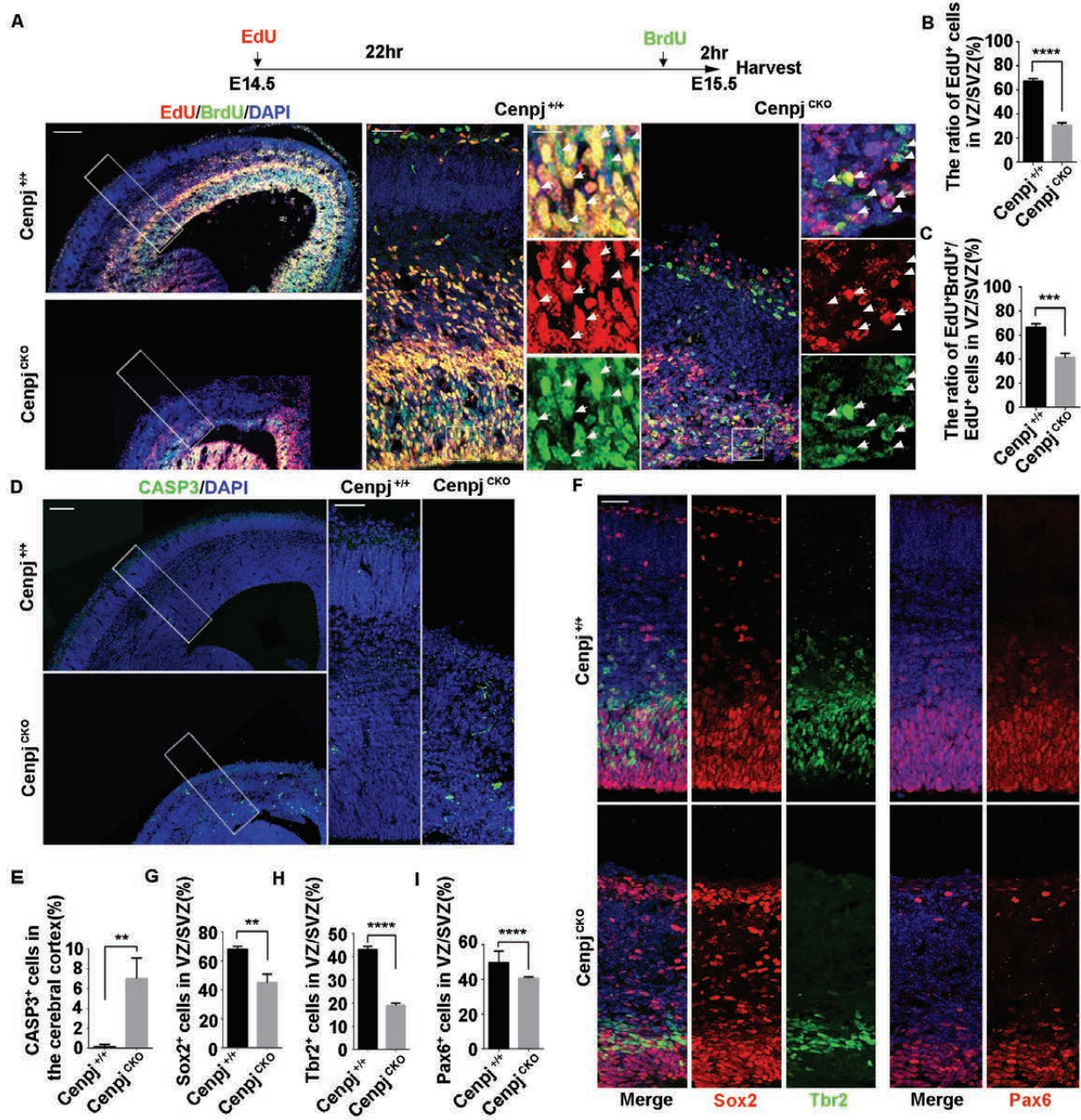


Figure 4

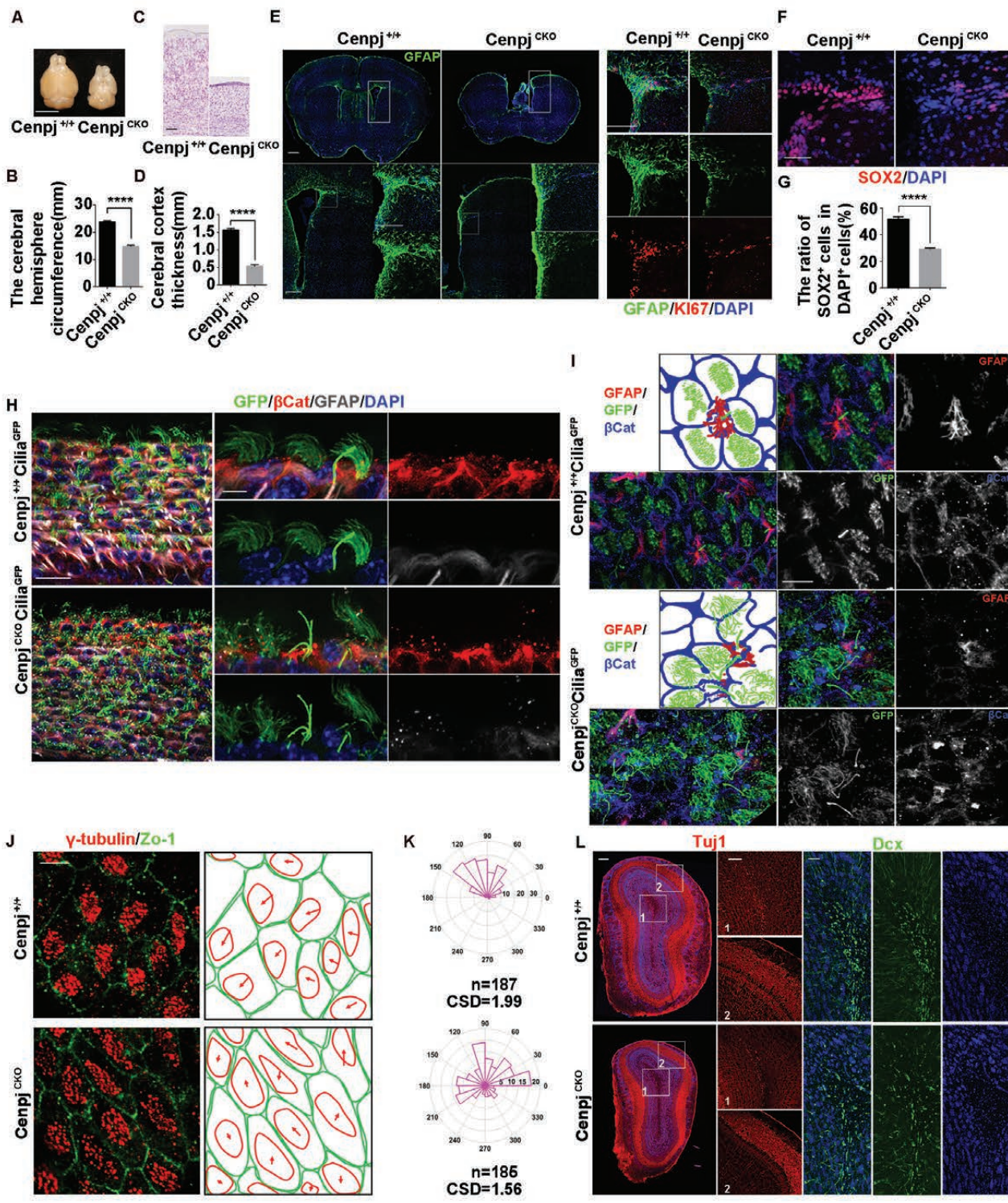


Figure 5

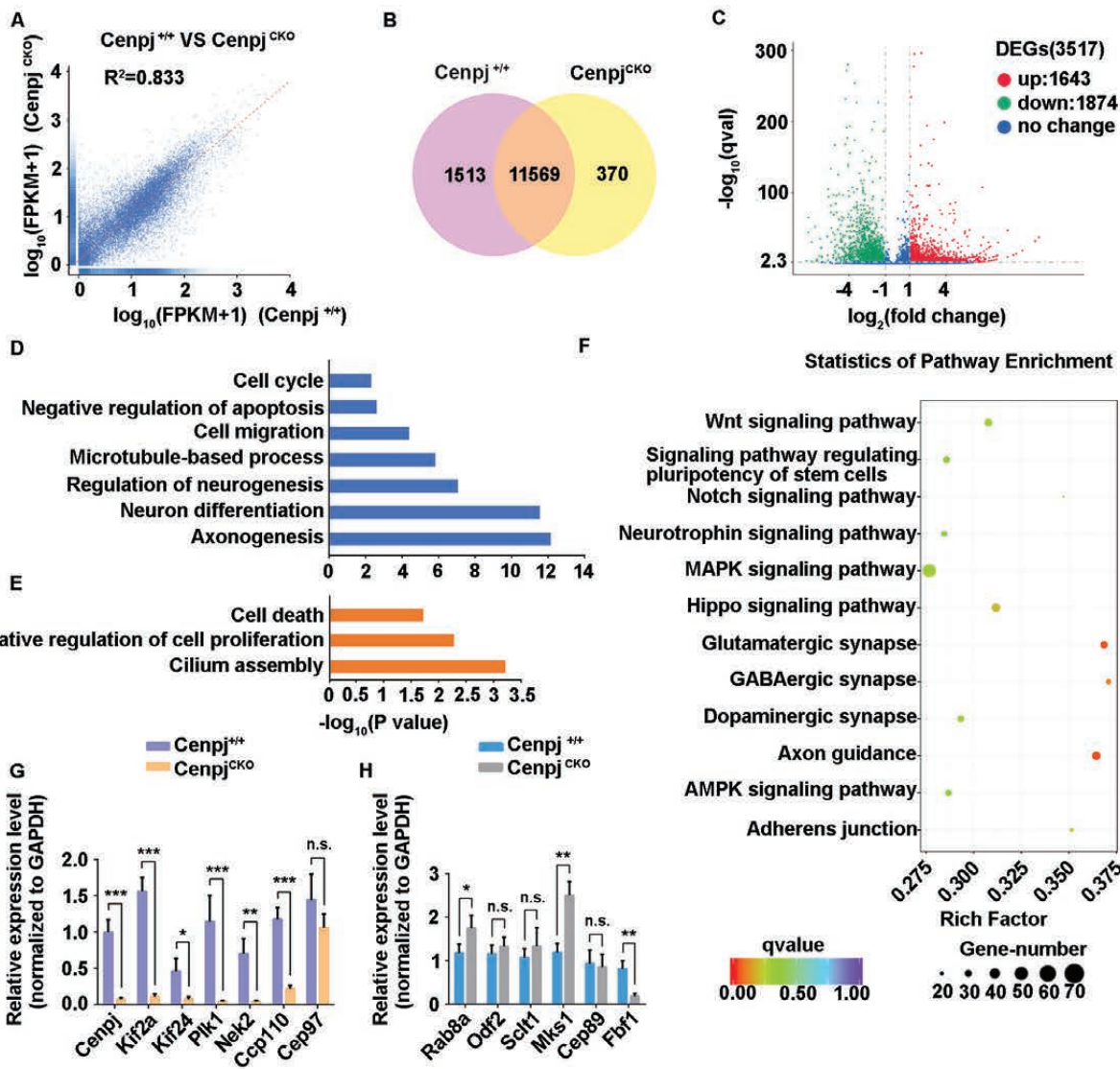


Figure 6

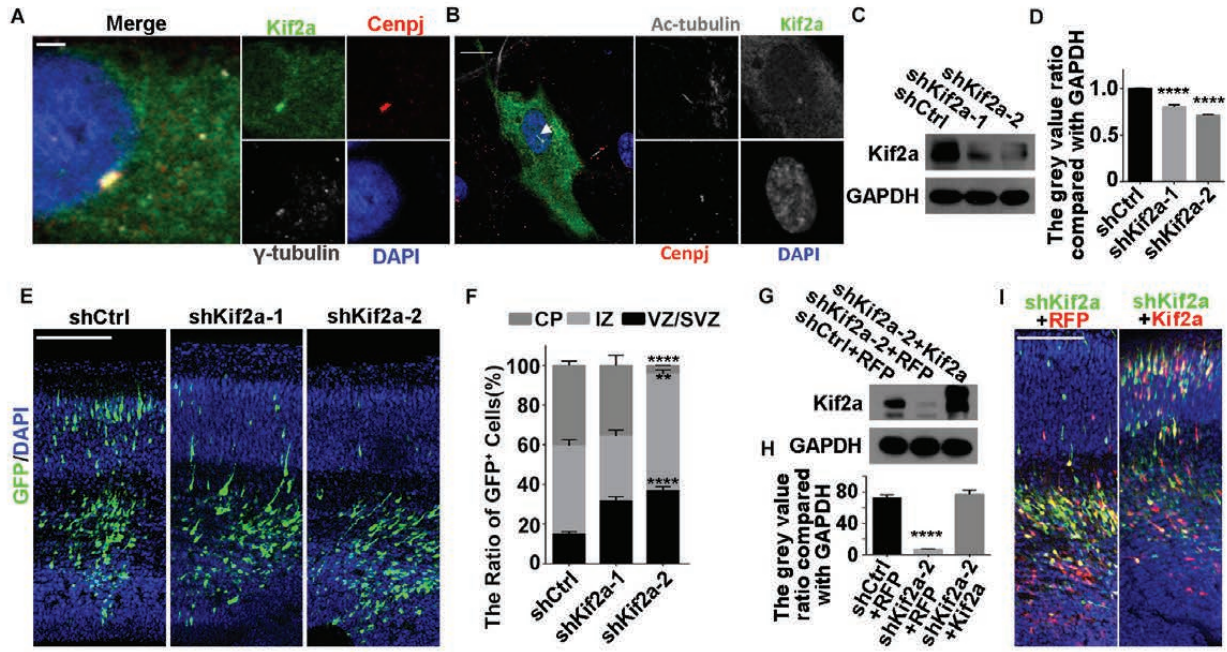


Figure 7

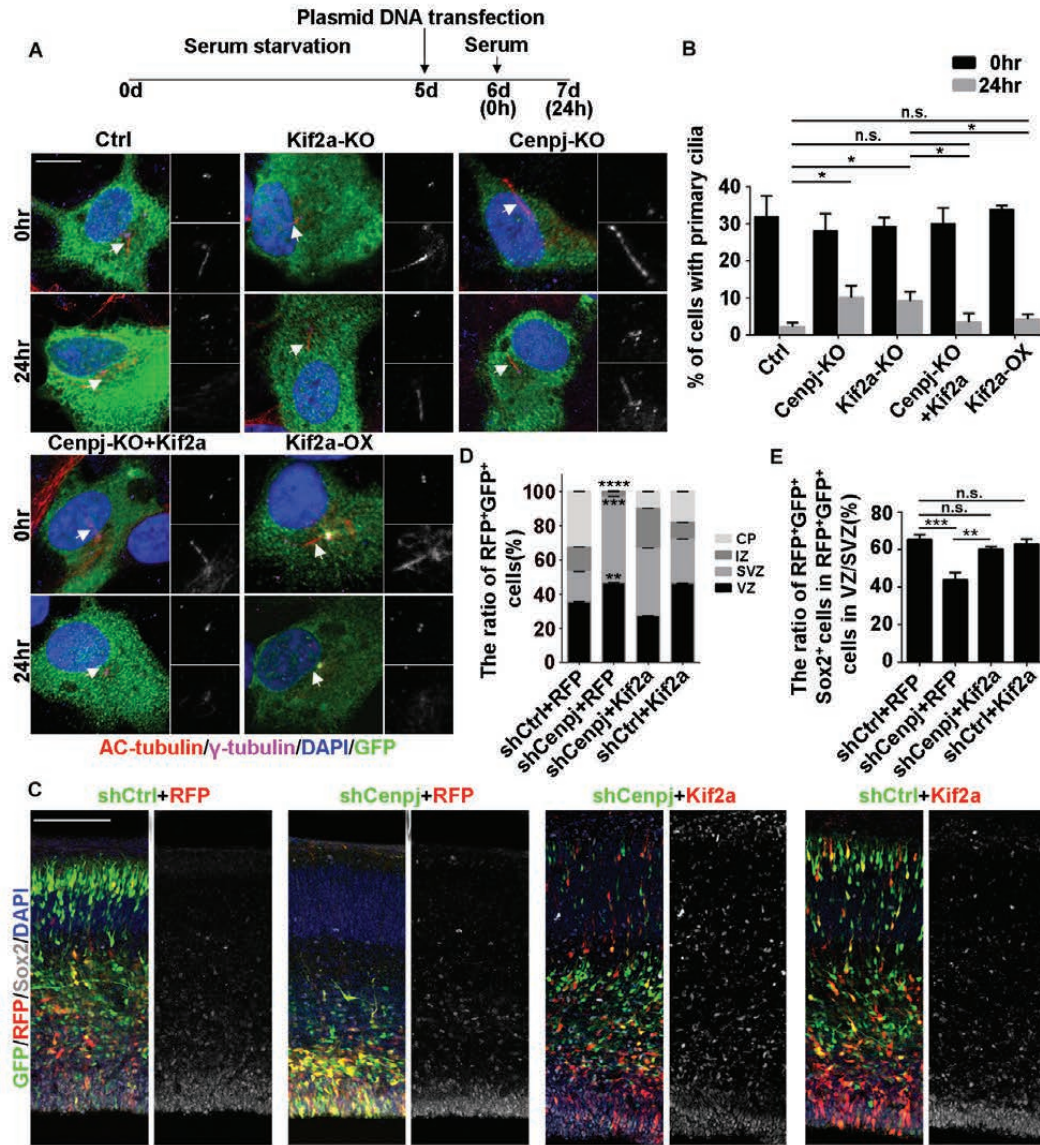


Figure 8

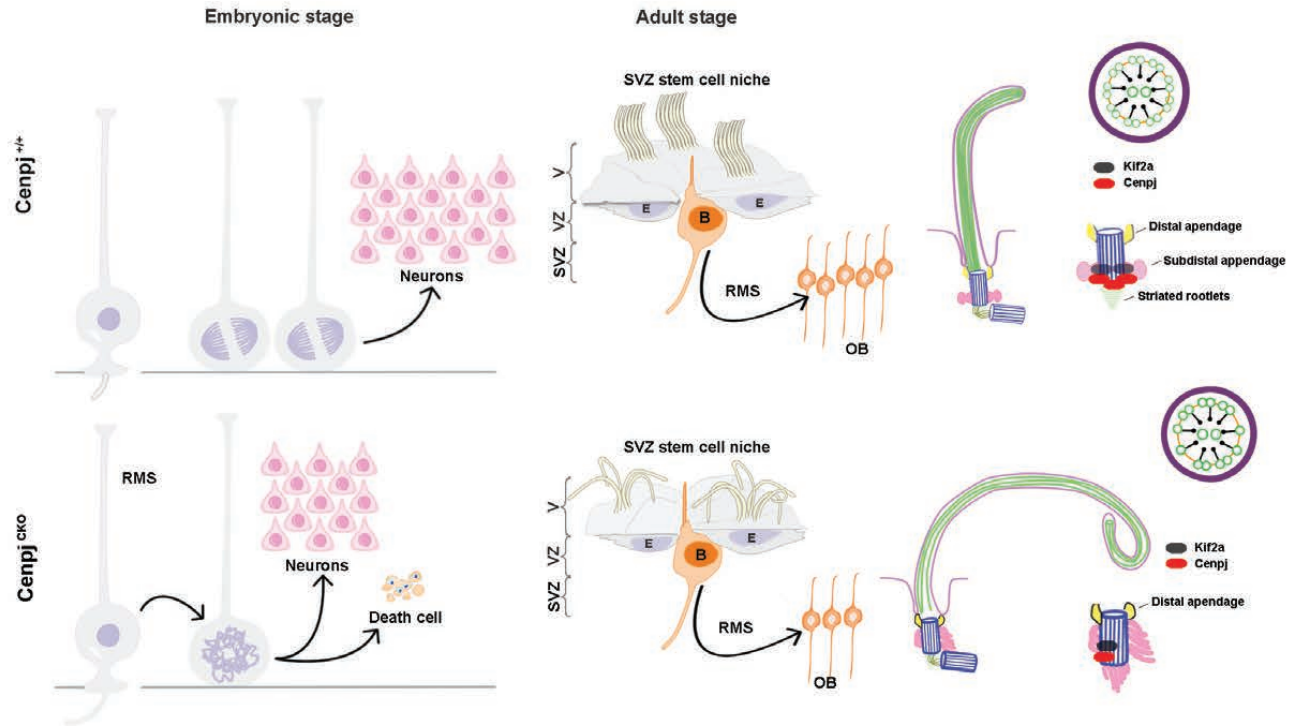


Figure 9